

Robust Implementation of Foreground Extraction and Vessel Segmentation for X-ray Coronary Angiography Image Sequence

Zeyu Fu^{a,b}, Zhuang Fu^{a,b,1,*}, Chenzhuo Lu^{a,b}, Jun Yan^{a,b}, Jian Fei^{c,d,e,f}, Hui Han^g

^aSchool of Mechanical Engineering, Shanghai Jiao Tong University, Shanghai 200240, China

^bState Key Laboratory of Mechanical System and Vibration, Shanghai 200240, China

^cDepartment of General Surgery, Pancreatic Disease Center, Ruijin Hospital, Shanghai Jiao Tong University School of Medicine, Shanghai 200025, China.

^dResearch Institute of Pancreatic Diseases, Shanghai Jiao Tong University School of Medicine, Shanghai 200025, China

^eState Key Laboratory of Oncogenes and Related Genes, Shanghai 200240, China

^fInstitute of Translational Medicine, Shanghai Jiao Tong University, Shanghai 200240, China.

^gDepartment of cardiovascular medicine, Ruijin Hospital, Shanghai Jiao Tong University School of Medicine, Shanghai 200025, China

Abstract

The extraction of contrast-filled vessels from X-ray coronary angiography (XCA) image sequence has important clinical significance for intuitively diagnosis and therapy. In this study, the XCA image sequence is regarded as a three-dimensional (3D) tensor input, vessel layer is regarded as a sparse tensor, and background layer is regarded as a low-rank tensor. Using tensor nuclear norm (TNN) minimization, a novel method for vessel layer extraction based on tensor robust principal component analysis (TRPCA) is proposed. Furthermore, considering the irregular movement of vessels and the dynamic interference of surrounding irrelevant tissues, the total variation (TV) regularized spatial-temporal constraint is introduced to separate the dynamic background. Subsequently, for the vessel images with uneven contrast distribution, a two-stage region growing (TSRG) method is utilized for vessel enhancement and segmentation. A global threshold segmentation is used as the preprocessing to obtain the main branch, and the Radon-Like features (RLF) filter is used to enhance and connect broken minor segments, the final vessel mask is constructed by combining the two intermediate results. The visibility of TV-TRPCA algorithm for foreground extraction and the accuracy of TSRG algorithm for vessel segmentation are evaluated on clinical XCA image sequences and third-party database. Both qualitative and quantitative results validate the superiority of the proposed method over the existing state-of-the-art approaches.

Keywords: X-ray coronary angiography, Tensor RPCA, TV regularization, Two-stage region growing, Layer extraction, Vessel segmentation

*Corresponding author at: School of Mechanical Engineering, Shanghai Jiao Tong University, 800 Dongchuan RD. Minhang District, Shanghai 200240, China. Email: zhfu@sjtu.edu.cn (Zhuang Fu)

¹Zeyu Fu and Zhuang Fu contributed equally to this work.

1. Introduction

Coronary artery disease (CAD) is one of the most deadly diseases globally[1]. Compared with drug therapy and surgical procedures such as coronary artery bypass grafting (CABG)[2], minimally invasive interventional surgery represented by percutaneous coronary intervention (PCI)[3] has become the main clinical means for the treatment of coronary artery disease with advantages of high precision, small wound and quick recovery. X-ray coronary angiography (XCA) is a method of imaging vessels under X-rays by injecting contrast agents. It can clearly display the anatomical structure of coronary artery, which has important clinical significance for pre-operative diagnosis and is also regarded as the gold standard[4]. XCA also plays a key role in multimodal registration[5], stenosis automatic assessment[6, 7], interventional path planning[8], coronary three-dimensional reconstruction[9, 10], stent implantation[11], and balloon angioplasty[12].

1.1. Background and Motivation

Although XCA can provide a fluoroscopic model of coronary arteries, it still has many aspects to be improved. (1) Peripheral irrelevant tissues such as ribs, spine, diaphragm and lung will also be developed by X-ray, resulting in low visibility of extracted vessels. (2) Images of different organs overlap after projection and affect the observation of lesions. (3) Different blood flow rates cause uneven distribution of contrast agents, and high-frequency Gaussian noise affects the detail performance of contrast images. See Fig.1. (a1).

Therefore, it is a prerequisite for accurate diagnosis and treatment to isolate background structure and noise signal from XCA image sequence to enhance vascular part. The purpose of this study is to extract the contrast-filled vessel layers from the original XCA image sequence and then perform accurate segmentation to restore the tubular structures.

1.2. Related Works and Methods

Methods of vessel extraction can be divided into three categories: vessel segmentation on features of a single image, digital subtraction angiography (DSA) on differentiated vessel masks, and vessel layer separation on continuous angiography image sequence.

Vessel segmentation is the most classical method, which is widely utilized in biomedical image processing. In practical application, in order to obtain better segmentation effect, it is often used in combination with other methods. Segmentation methods based on vessel enhancement, deformable models, tracking approaches and machine learning are the commonly used[14]. Considering the characteristics of vascular tubular structure, most vessel enhancement methods realize multi-scale filtering enhancement of vessel region by constructing different vascular model response functions for convolution processing based on Hessian matrix eigenvalues. Commonly used vascular model functions include Frangi[15], Sato[16], Erdt[17], etc. Different from Hessian matrix filter, the method of Radon-like features (RLF) filter[18] has been proposed in recent years. It is based on edge sensing in different directions to make non-isotropic sampling of the neighborhood, which can highlight the coronary artery more completely, including minor segments. Syeda-Mahmood adopted RLF filter for vessel enhancement in coronary image segmentation and achieved

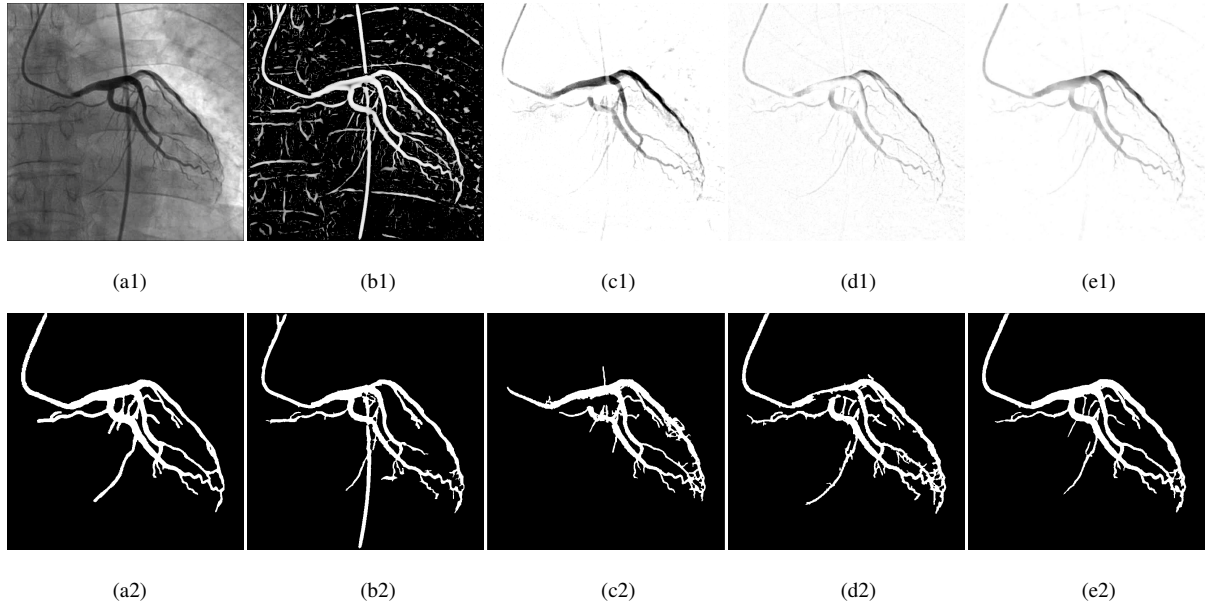


Figure 1: Methods of vessel extraction. (a1)-(a2) are the original XCA image and its ground truth vessel mask selected by the surgeon. (b1)-(b2) are the multi-scale Frangi filtering vessel enhancement and its segmentation by region growing. (c1)-(c2) are the vessel layer extracted by DSA and its segmentation. (d1)-(d2) are the vessel layer extracted by TNN-TRPCA[13] method and its segmentation. (e1)-(e2) are the vessel layer extracted by proposed TV-TRPCA method and its segmentation. The vessel segmentation of (c1)-(e1) is based on the proposed two-stage region growing method.

remarkable results[19]. However, a variety of noise signals are also enhanced at the same time. Generally, threshold segmentation methods such as OTSU[20] or maximum entropy[21] are used for postprocessing to obtain a high signal-to-noise ratio (SNR) vessel mask. Fig.1. (b1) (b2) show the vessel enhancement by multi-scale Frangi filtering and the corresponding vessel segmentation result. The advantage of vessel enhancement is that no prior model is required, but it remains artifacts and irrelevant tissues. Moreover, thick blood vessels are prone to cavities, so appropriate parameters must be selected for vessels of different gray scales and thicknesses, resulting in poor portability. The method based on deformable models extract vessels by selecting the appropriate initial vascular model. It is more suitable for medical images with complex background by combining prior information and utilizing the grayscale, gradient, texture and other characteristics of images. This algorithm can be divided into two categories: boundary-based and region-based. Typical boundary-based deformable models include B-Snake model[22], Level set model[23] and Active shape model[24]. Region-based deformable vessel segmentation algorithm selects seed points inside vessels as the starting point of region growing and expands continuously by traversing the surrounding voxel points. Kerkeni[25] and Sui[7] implemented coronary artery segmentation in XCA images using multi-scale region growing algorithm. Most model-based methods are semi-automatic and sensitive to the selection of initial models, vessel enhancement is usually used as preprocessing to improve segmentation accuracy. Tracking approaches are divided into model-based and least-cost-path-based. It starts from the seed point and grows iteratively along a certain location and direction according to preset constraints to obtain a tubular structure[26] (model-based) or a centerline tree[27]

(least-cost-path-based). This method is more frequently used in the extraction of vessel centerline. The method based on machine learning has the widest application scope in vessel segmentation. It does not need to extract features from original images and can judge the contour of vessels adaptively. At present, machine learning methods with high accuracy such as fully convolutional networks (FCN)[28, 29] and U-Net[30, 31] are supervised, the training and template marking are cumbersome.

Digital subtraction angiography (DSA)[32] is a technique to highlight blood vessels by eliminating bones and soft tissues from angiographic images by subtraction. The vessel region can be defined by the difference between mask images before and after angiography. Due to the breathing and movement of human body, direct subtraction will produce motion artifacts. In order to obtain the spatial-temporal corresponding initial mask image, Bentoutou[33, 34] improved the image registration method, Yamamoto[35] proposed the threshold adaptive search method, and Song[36] adopted the patch-based adaptive background subtraction method, both of which achieved certain results. Fig.1. (c1) (c2) show the vessel layer extracted by DSA and its segmentation result. The spatial and temporal consistency of the initial mask of DSA could be seriously disturbed by vessel movements and contrast agent distribution changes, high-frequency noise and dynamic background will also affect its calculation accuracy.

Layer separation is a video segmentation algorithm commonly used in machine vision. It regards the scene in the video as the superposition of multiple element layers such as foreground, background and noise, then extracts different layers separately. In XCA image sequence, different tissues have different motion patterns. Coronary artery motion is the most intense and irregular, lung respiration is slow and uniform, ribs and diaphragm move periodically with lung respiration, and spine remains basically static. Therefore, vessel layers can be extracted by layer separation. Different from the filtering method which simply enhances the vessel pixel mathematically, the layer separation algorithm can obtain the image sequence that truly reflects the continuous motion information of vessels. Neural network-based method and dimension reduction based method have been applied in vessel layer separation. Data-driven deep learning networks with different training strategies such as convolutional neural networks (CNN)[37], FCN[38] and U-Net[39] have been proposed to extract vessel layers and enhance vessel structures. The neural network-based method extracts vessel features from the training set marked in advance and applies them to the test set, which can distinguish the background tissue and vessel layer well. However, this method is difficult to accurately separate vessel and tubular noise, and the debugging of network parameters is also a tedious and time-consuming work. The method based on dimension reduction does not require prior knowledge, nor does it need to estimate the motion of vessels by frame, so it has higher efficiency in XCA image layer separation. Tang[40] used independent component analysis (ICA) to separate coronary artery and background in DSA, which has the advantage of being more continuous than traditional subtraction, but the registration accuracy of the initial mask is limited by the dynamic background. Xia[41] proposed a matrix decomposition model (MDM) with gradient sparsity to capture and segment blood vessels through container framework. The theory decomposed non-vessel background into static background structure, background structure away from blood vessels and background structure close to vessels, achieving certain effects on XCA image sequences with complex backgrounds. However, this method will delete a large number of broken vascular segments similar to

the background structure and cannot completely display the coronary tree.

Robust principal component analysis (RPCA)[42] is a typical dimension reduction method with global low-rank property. The original observation matrix $\mathbf{O} \in \mathbb{R}^{MN \times T}$ is quantized and superimposed, the low-rank matrix $\mathbf{B} \in \mathbb{R}^{MN \times T}$ represents the static background and the sparse matrix $\mathbf{L} \in \mathbb{R}^{MN \times T}$ represents the moving foreground. The iterative decomposition operation is carried out by minimizing the cost function. A typical RPCA solution algorithm via principal component pursuit (PCP)[43] can be calculated according to Eq.1

$$\min_{\mathbf{B}, \mathbf{L}} \|\mathbf{B}\|_* + \lambda \|\mathbf{L}\|_1 \quad s.t. \quad \mathbf{O} = \mathbf{B} + \mathbf{L} \quad (1)$$

where $\|\mathbf{B}\|_* = \sum \sigma(\mathbf{B})$ is the nuclear norm of matrix \mathbf{B} , which is the sum of all singular values, $\|\mathbf{L}\|_1 = \sum_{i,j} |\mathbf{L}_{i,j}|$ is the ℓ_1 norm of \mathbf{L} , which is the sum of absolute values of all elements, λ is a positive scalar equilibrium factor for balancing foreground and background. In recent years, RPCA and its derivative algorithms have been widely utilized in XCA image layer separation. Ma[44] decomposed XCA images into three layers by using morphological filtering superimposed RPCA method, which significantly improved the visibility of blood vessels. On this basis, an automatic online layer separation method was designed to guide PCI surgery[45]. Zhang[46] proposed a vesselness-constrained RPCA approach (VC-RPCA) that incorporated the vessel-like appearance into the layer separation framework to achieve precise vessel enhancement, and an adaptive regularization strategy is used to capture vessels without significant movement. Qin[47] performed global logarithmic transformation on XCA images, used IALM-RPCA to separate layers in logarithmic space, and restored the background layer by tensor completion. This method replaced addition operation with multiplication operation in the original image space, which is more consistent with the physical model of XCA. Song[48] integrated the motion consistency of quasi-static structure and the smoothness of blood vessels into the layer separation of XCA image sequence, and proposed an online RPCA method adaptively calculated spatial constraints using the proportion of the vascular region in the previous frame, which can retain the local blood vessel information after the contrast agent dissipates.

The RPCA in matrix form above has one disadvantage: it can only process two-dimensional data. However, the actual data is usually high-dimensional in nature, so to use RPCA, the original data must be matricized first, but matricization will destroy its inherent spatial structure, resulting in information loss and performance degradation. In addition, the results obtained after video matricization become huge, which occupies a large memory space and increases the computational complexity. To solve this problem, convex optimization method tensor robust principal component analysis (TRPCA) was introduced for low-rank tensor decomposition (LRTD). Since tensor rank[49, 50, 51, 13] can be defined as CP-rank based on CANDECOMP/PARAFAC (CP) decomposition, Tucker-rank based on higher-order principal component analysis (HOPCA), Tubal-rank, Multi-rank and Average-rank based on higher-order singular value decomposition (HOSVD), etc., various TRPCA methods have been extended. In order to reduce the loss of high-dimensional information, Goldfarb[52] proposed high-order RPCA (HoRPCA) model. Xie[53] proposed Kronecke-Basis-Representation based RPCA (KBR-RPCA) model, which uses tensor sparse detection to replace the

background of nuclear norm modeling, and assigns appropriate weights to the rank of each dimension. Liu[54] proposed a new tensor nuclear norm for background constraint based on low-rank components of core tensors, which improved the accuracy of foreground background separation. Driggs[55] used atomic norm regularization to provide better recovery for tensor-structured data sets, and built a nonconvex model to recover tensors with CP-rank much larger than all side lengths. Lu[56, 13] proposed an improved tensor nuclear norm TRPCA (TNN-TRPCA) model for background modeling to strengthen the low-rank property of background. Gao[57] applied the weighted Schatten p -norm minimization (WSNM)[58] model for LRTD and proposed an enhanced TRPCA (ETRPCA) algorithm, which further improved the stability of background modeling in complex fields. Most of the above methods adopt ℓ_1 norm constraint for foreground, but ℓ_1 norm treats each pixel independently without considering the spatial continuity and temporal persistence of foreground target, which makes the algorithm insensitive to the discontinuous moving foreground and dynamic background. RPCA and TRPCA algorithms with ℓ_1 norm regularization constraint are difficult to avoid blurred edges and internal cavities in moving object detection, shown in Fig.1. (d1) (d2).

Total variation (TV) regularization can compensate for the deficiency of ℓ_1 norm, it improves the spatial-temporal continuity of foreground layer and the spatial-temporal correlation of background layer in LRTD. Chan[59] proposed a total variation norm regularization method based on ℓ_1 norm and $\ell_{2,1}$ norm for video deblurring, denoising and disparity refinement, where ℓ_1 norm and $\ell_{2,1}$ norm correspond to isotropic and anisotropic inputs respectively. This method has been widely promoted in recent works[60, 61, 62, 63], it has a strong inhibitory effect on discontinuous changes, effectively inhibits the interference of dynamic background to foreground extraction, and makes layer separation more accurate. Jin[64] introduced total variation regularization into the foreground extraction of XCA video and proposed the motion coherent regularization RPCA (MCR-RPCA), which improved the motion continuity of vessel layer without the benefit of prior knowledge. However, this method still needs to matricize the video, which destroys the original spatial structure and cannot naturally retain the high-dimensional spatial-temporal information obtained by angiography.

1.3. Main Contributions

Before presenting our method, it is necessary to discuss the characteristics of XCA image sequences. Different from general moving object detection, the moving foreground objects (blood vessels) in XCA video will gradually extend various branches over time, and they move irregularly with the heartbeat rather than the common translatory motion, so the vessel layer tensor is not completely sparse. The dynamic background moves with respiration and has a low frequency, which can be regarded as a sparse tensor. At the same time, in XCA video, the proximal vessel branches are visually thick and have small motion amplitude, meanwhile the distal vessel branches are visually thin and have large motion amplitude. The vessel layer extracted by layer separation will have uneven gray distribution and local fracture, which will affect the accuracy of subsequent quantitative analysis.

To solve the above problems, we propose a total variation regularized tensor robust principal component analysis (TV-TRPCA) method to extract the contrast-filled vessel mask. The model regards XCA sequence as the superposition

of vessel layer, static background layer, dynamic background layer and noise layer, uses the tensor nuclear norm (TNN) minimization to constrain the background and TV/ℓ_1 norm regularization to constrain the foreground, which strengthen the low-rank property of the background and the spatial-temporal continuity of the foreground. Moreover, a two-stage region growing (TRSG) method is used to enhance and segment the vessels extracted by layer separation. To the best of our knowledge, we are the first to apply TRPCA to XCA vessel layer separation. Comparing with the existing RPCA-based methods, the recovery of high-dimensional spatial-temporal information is more accurate. The result of foreground extraction and vessel segmentation is shown in Fig.1. (e1) (e2).

The main contributions of this paper are as follows:

(1) We propose a total variation regularized tensor robust principal component analysis (TV-TRPCA) method, which effectively improves the visibility of XCA image sequence foreground extraction.

(2) We adopt a two-stage regional growing method to segment the extracted contrast-filled vessels. Specifically, the main branch was obtained by global threshold segmentation, and the minor vessel segments were enhanced and connected by Radon-Like features (RLF) filter. Finally, an accurate binary vessel mask was obtained.

The rest of this paper is organized as follows. In Section 2, the proposed TV-TRPCA model and TRSG algorithm are introduced in detail. The experimental results, including a thorough comparison and detailed analysis of the method performance, are presented in Section 3. The Section 4 gives the conclusion.

2. Methods

In this section, we will introduce the theory of tensor robust principal component analysis, total variation, and some vessel enhancement and segmentation methods.

2.1. Foreground Extraction

2.1.1. Basic Definitions and Notations of Tensors

In this paper, tensors are denoted by Euler script letters, e.g., \mathcal{X} . Matrices are denoted by boldface capital letters, e.g., \mathbf{X} , vectors are denoted by boldface lowercase letters, e.g., \mathbf{x} , and scalars are denoted by lowercase letters, e.g., x . For a 3-D tensor in the field of real numbers denoted as $\mathcal{X} \in \mathbb{R}^{M \times N \times T}$, in which M, N, T are the side lengths of each dimension, some used 3-D tensor notations are summarized in Tab.1. In which $X_{mt} \in \mathbb{R}$ is a scalar, $\mathcal{X}^{(t)} \in \mathbb{R}^{M \times N}$ is a matrix, $\text{Vec}(\mathcal{X}) \in \mathbb{R}^{MNT}$ is a vector, $\widetilde{\mathcal{X}} \in \mathbb{C}^{M \times N \times T}$ is the Discrete Fourier Transformation(DFT) on \mathcal{X} along the 3-rd dimension. $\langle \mathbf{X}, \mathbf{Y} \rangle = \text{Tr}(\mathbf{X}^* \mathbf{Y})$ represents the inner product of two matrices. $\text{bcirc}(\mathcal{X}) \in \mathbb{R}^{MT \times NT}$ and $\text{bstack}(\mathcal{X}) \in \mathbb{R}^{MT \times N}$ are two tensor operators as defined below.

Table 1: Notations of 3-D Tensors[56, 13, 60, 50, 65]

Notations	Explanations
$\mathcal{X}, \mathbf{X}, \mathbf{x}, x$	tensor, matrix, vector, scalar
$\mathcal{X}(m, n, t)$ or X_{mnt}	the $(m, n, t)^{th}$ entry of \mathcal{X}
$\mathcal{X}(m, :, :), \mathcal{X}(:, n, :), \mathcal{X}(:, :, t)$	the m^{th}, n^{th}, t^{th} horizontal, lateral and frontal slice of \mathcal{X}
$\mathcal{X}^{(t)}$	the t^{th} frontal slice of \mathcal{X}
$\ \mathcal{X}\ _1 = \sum_{m,n,t} X_{mnt} $	ℓ_1 norm of \mathcal{X}
$\ \mathcal{X}\ _F = \sqrt{\sum_{m,n,t} X_{mnt} ^2}$	Frobenius norm of \mathcal{X}
$\langle \mathcal{X}, \mathcal{Y} \rangle = \sum_{t=1}^T \langle \mathcal{X}^{(t)}, \mathcal{Y}^{(t)} \rangle$	inner product of \mathcal{X} and \mathcal{Y}
$\mathcal{X} * \mathcal{Y} = fold(bcirc(\mathcal{X}) \cdot bstack(\mathcal{Y}))$	tensor product of \mathcal{X} and \mathcal{Y}
$\mathbf{Vec}(\mathcal{X})$ or $f(\mathcal{X})$	vectorization of \mathcal{X}
$\tilde{\mathcal{X}} = \mathbf{fft}(\mathcal{X}, [1, 3])$	DFT on \mathcal{X} along the 3-rd dimension
$rank_a(\mathcal{X}) = \frac{1}{T} rank(bcirc(\mathcal{X}))$	tensor average rank
$\ \mathcal{X}\ _{\otimes} = \frac{1}{T} \sum_{t=1}^T \ \tilde{\mathcal{X}}^{(t)}\ _*$	tensor nuclear norm of \mathcal{X}

$bcirc(\mathcal{X})$ is the block circulant matrix formed by circular combination of the frontal slice of tensor \mathcal{X} :

$$bcirc(\mathcal{X}) = \begin{bmatrix} \mathcal{X}^{(1)} & \mathcal{X}^{(T)} & \dots & \mathcal{X}^{(2)} \\ \mathcal{X}^{(2)} & \mathcal{X}^{(1)} & \dots & \mathcal{X}^{(3)} \\ \vdots & \vdots & \ddots & \vdots \\ \mathcal{X}^{(T)} & \mathcal{X}^{(T-1)} & \dots & \mathcal{X}^{(1)} \end{bmatrix}$$

Compared with matricizations along certain dimension, the block circulant matricization can preserve more spatial relationship among entries[56].

$bstack(\mathcal{X})$ is the block stacking matrix formed by stacking the frontal slice of tensor \mathcal{X} and $fold(\cdot)$ is the inverse

operator:

$$bstack(\mathcal{X}) = \begin{bmatrix} \mathcal{X}^{(1)} \\ \mathcal{X}^{(2)} \\ \vdots \\ \mathcal{X}^{(T)} \end{bmatrix}, \quad fold(bstack(\mathcal{X})) = \mathcal{X}$$

The conjugate transpose of complex tensor $\mathcal{X} \in \mathbb{C}^{M \times N \times T}$ is the tensor $\mathcal{X}^* \in \mathbb{C}^{N \times M \times T}$ obtained by conjugate transposing each of the frontal slices and then reversing the order of transposed frontal slices 2 through T [13].

The identity tensor $\mathcal{I} \in \mathbb{R}^{M \times M \times T}$ is a tensor whose first frontal slice is a $M \times M$ identity matrix, and other frontal slices are all zeros[65].

A complex tensor $\mathcal{Q} \in \mathbb{C}^{M \times M \times T}$ is unitary if it satisfies $\mathcal{Q}^* * \mathcal{Q} = \mathcal{Q} * \mathcal{Q}^* = \mathcal{I}$. The unitary tensor expands orthogonal tensor[65] in the complex field.

The f-diagonal tensor is a tensor with each frontal slice being diagonal matrix[65].

2.1.2. T-SVD

For $\mathcal{X} \in \mathbb{C}^{M \times N \times T}$, it can be factorized as

$$\mathcal{X} = \mathcal{U} * \mathcal{S} * \mathcal{V}^* \quad (2)$$

where $\mathcal{U}, \mathcal{V} \in \mathbb{C}^{M \times M \times T}$ are unitary tensors, $\mathcal{S} \in \mathbb{R}^{M \times N \times T}$ is an f-diagonal positive real tensor. Eq.2 is called the tensor singular value decomposition (t-SVD)[65]. In order to compute t-SVD, it is supposed to analyze the properties of tensor product (t-product) first.

Based on circular combination and stacking operations, the tensor product can be defined as follows:

$$\mathcal{Z} = \mathcal{X} * \mathcal{Y} = fold(bcirc(\mathcal{X}) \cdot bstack(\mathcal{Y})) \quad (3)$$

where $\mathcal{Y} \in \mathbb{R}^{N \times L \times T}$ and $\mathcal{Z} \in \mathbb{R}^{M \times L \times T}$. The t-product has a similar form to matrix products except that cyclic convolution replaces the product operation of elements, it acts on tensors in the original domain which corresponds to the matrix product of the frontal slices in the Fourier domain[65]:

$$\tilde{\mathcal{Z}}^{(t)} = \tilde{\mathcal{X}}^{(t)} * \tilde{\mathcal{Y}}^{(t)}, \quad t = 1, 2, \dots, T. \quad (4)$$

Based on this property, t-SVD can be computed in Fourier domain efficiently. Specifically, each frontal slice of $\tilde{\mathcal{U}}, \tilde{\mathcal{S}}$ and $\tilde{\mathcal{V}}$ can be solved by matrix singular value decomposition:

$$[\tilde{\mathcal{U}}^{(t)}, \tilde{\mathcal{S}}^{(t)}, \tilde{\mathcal{V}}^{(t)}] = \mathbf{SVD}(\tilde{\mathcal{X}}^{(t)}), \quad t = 1, 2, \dots, T. \quad (5)$$

Finally, $\mathcal{U}, \mathcal{S}, \mathcal{V}$ can be computed by performing inverse DFT on $\tilde{\mathcal{U}}, \tilde{\mathcal{S}}, \tilde{\mathcal{V}}$ obtained in Eq.5 along the 3-rd dimension:

$$\mathcal{J} = \mathbf{ifft}(\tilde{\mathcal{J}}, [1, 3]), \quad \mathcal{J} = \mathcal{U}, \mathcal{S}, \mathcal{V} \quad (6)$$

2.1.3. Tensor Nuclear Norm

In robust principal component analysis (RPCA), low-rank constraint and sparse constraint are applied to the background and foreground. But the computation of matrix rank and ℓ_0 norm is NP-hard in mathematics. In practice, these two terms are generally convex relaxed by nuclear norm and ℓ_1 norm, and the object is transformed into a convex optimization problem. This approach can be extended to tensor robust principal component analysis (TRPCA).

In this paper, we adopted tensor average rank and its tight convex surrogate tensor nuclear norm (TNN) for low-rank tensor recovery[56, 13]. For $\mathcal{X} \in \mathbb{R}^{M \times N \times T}$, the tensor average rank can be defined as

$$\mathbf{rank}_a(\mathcal{X}) = \frac{1}{T} \mathbf{rank}(bcirc(\mathcal{X})) \quad (7)$$

According to [13], a low tubal rank tensor always has low average rank, and the low average rank assumption is weaker than the low Tucker-rank and low CP-rank assumptions. Thus the low-rank property of background can be strengthened by using tensor average rank.

The tensor nuclear norm of $\mathcal{X} \in \mathbb{R}^{M \times N \times T}$ is defined as the average of the nuclear norm of all the frontal slices of $\tilde{\mathcal{X}}$ in Fourier domain, it is also closely related to the nuclear norm of the block circulant matrix $bcirc(\mathcal{X})$ in the original domain[56], i.e.,

$$\|\mathcal{X}\|_{\otimes} = \frac{1}{T} \sum_{t=1}^T \|\tilde{\mathcal{X}}^{(t)}\|_* = \frac{1}{T} \|bcirc(\mathcal{X})\|_* \quad (8)$$

2.1.4. Total Variation

Total variation (TV) was first proposed in [66] to solve image denoising problems. Since then, TV model has been widely used in many computer vision (CV) problems.

In XCA image sequence, the trajectory of vessel foreground is usually smooth in time and space domain, while the significant change of dynamic disturbance is discontinuous. In mathematics, total variation can smooth the signal and restrain the discontinuous change[60]. Therefore, TV regularization can effectively suppress the interference caused by dynamic background. Pixel gradient regards the XCA images as a discrete function, which can be used as the approximation to variation. Suppose the vessel foreground tensor is $\mathcal{H} \in \mathbb{R}^{M \times N \times T}$, we can represent its horizontal, vertical, and temporal variances as

$$\begin{cases} \nabla_m \mathcal{H}(m, n, t) = \mathcal{H}(m+1, n, t) - \mathcal{H}(m, n, t) \\ \nabla_n \mathcal{H}(m, n, t) = \mathcal{H}(m, n+1, t) - \mathcal{H}(m, n, t) \\ \nabla_t \mathcal{H}(m, n, t) = \mathcal{H}(m, n, t+1) - \mathcal{H}(m, n, t) \end{cases} \quad (9)$$

$m = 1, 2, \dots, M; n = 1, 2, \dots, N; t = 1, 2, \dots, T$

To avoid data overflow, define $\mathcal{H}(M+1, n, t) = \mathcal{H}(1, n, t)$, $\mathcal{H}(m, N+1, t) = \mathcal{H}(m, 1, t)$, $\mathcal{H}(m, n, T+1) = \mathcal{H}(m, n, 1)$. The total variation of \mathcal{H} , denoted as $\nabla \mathcal{H} \in \mathbb{R}^{M \times N \times 3T}$, is defined as the weighted superposition of variance in each dimension:

$$\nabla \mathcal{H} = fold \left(\left[\sigma_m \mathbf{H}_m^T, \sigma_n \mathbf{H}_n^T, \sigma_t \mathbf{H}_t^T \right]^T \right) = fold(\mathbf{H}) \quad (10)$$

where $\sigma_m, \sigma_n, \sigma_t$ are the scalar weights of each dimension, $\mathbf{H}_m, \mathbf{H}_n, \mathbf{H}_t \in \mathbb{R}^{MT \times N}$ are the block stacking matrices of $\nabla_m \mathcal{H}, \nabla_n \mathcal{H}, \nabla_t \mathcal{H} \in \mathbb{R}^{M \times N \times T}$, i.e.,

$$\mathbf{H}_i = \text{bstack}(\nabla_i \mathcal{H}), \quad i = m, n, t$$

Since the $\ell_{2,1}$ norm based sparsity constraint forcing exact zero columns or rows, it is not suitable for anisotropic inputs such as XCA image sequence[64]. Therefore, we adopt TV/ℓ_1 norm to constrain the foreground total variation, based on Eq.10, it can be computed as

$$\begin{aligned} \|\mathcal{H}\|_{TV1} &= \sigma_m \|\nabla_m \mathcal{H}\|_1 + \sigma_n \|\nabla_n \mathcal{H}\|_1 + \sigma_t \|\nabla_t \mathcal{H}\|_1 \\ &= \|\nabla \mathcal{H}\|_1 \end{aligned} \quad (11)$$

2.1.5. TV-TRPCA

On the basis of the previous definitions, in this section we will derive the total variation regularized tensor robust principal component analysis (TV-TRPCA) in detail.

First the original grayscale image sequence is normalized into a 3-D tensor $\mathcal{O} \in \mathbb{R}^{M \times N \times T}$, M, N are image height and width, T is the number of frames. In ideal cases, \mathcal{O} is the superposition of low-rank static background tensor $\mathcal{B} \in \mathbb{R}^{M \times N \times T}$, Gaussian noise tensor $\mathcal{G} \in \mathbb{R}^{M \times N \times T}$ and residual completely sparse foreground (Laplacian noise) tensor $\mathcal{R} \in \mathbb{R}^{M \times N \times T}$ [67]. In TRPCA with convex relaxation, $\mathcal{B}, \mathcal{R}, \mathcal{G}$ can be achieved through minimizing the following problem:

$$\min_{\mathcal{B}, \mathcal{R}, \mathcal{G}} \|\mathcal{B}\|_{\otimes} + \lambda_1 \|\mathcal{R}\|_1 + \frac{\lambda_2}{2} \|\mathcal{G}\|_F^2 \quad s.t. \quad \mathcal{O} = \mathcal{B} + \mathcal{R} + \mathcal{G} \quad (12)$$

where λ_1, λ_2 are positive scalar equilibrium factors.

The above decomposition works well assuming that the background is completely stationary. However, according to the previous analysis, there exists non-negligible low-frequency dynamic background in XCA video, which makes the accuracy of Eq.12 decline sharply. In fact, the nonzero entries in \mathcal{R} are consisted of two components, the vessel foreground $\mathcal{H} \in \mathbb{R}^{M \times N \times T}$ and dynamic background $\mathcal{E} \in \mathbb{R}^{M \times N \times T}$. Therefore, we can update Eq.12 into a more accurate form:

$$\begin{aligned} \min_{\mathcal{B}, \mathcal{R}, \mathcal{G}, \mathcal{E}, \mathcal{H}} \|\mathcal{B}\|_{\otimes} + \lambda_1 \|\mathcal{R}\|_1 + \frac{\lambda_2}{2} \|\mathcal{G}\|_F^2 + \lambda_3 \|\mathcal{E}\|_1 + \lambda_4 \|\mathcal{H}\|_{TV1} \\ s.t. \quad \mathcal{O} = \mathcal{B} + \mathcal{R} + \mathcal{G}, \quad \mathcal{R} = \mathcal{E} + \mathcal{H} \end{aligned} \quad (13)$$

where $\lambda_1, \lambda_2, \lambda_3, \lambda_4$ are positive scalar equilibrium factors. Considering $\|\mathcal{H}\|_{TV1} = \|\nabla \mathcal{H}\|_1$, let $\mathcal{T} \in \mathbb{R}^{M \times N \times 3T} = \nabla \mathcal{H}$, then Eq.13 can be converted to

$$\begin{aligned} \min_{\mathcal{B}, \mathcal{R}, \mathcal{G}, \mathcal{E}, \mathcal{H}, \mathcal{T}} \|\mathcal{B}\|_{\otimes} + \lambda_1 \|\mathcal{R}\|_1 + \frac{\lambda_2}{2} \|\mathcal{G}\|_F^2 + \lambda_3 \|\mathcal{E}\|_1 + \lambda_4 \|\mathcal{T}\|_1 \\ s.t. \quad \mathcal{O} = \mathcal{B} + \mathcal{R} + \mathcal{G}, \quad \mathcal{R} = \mathcal{E} + \mathcal{H}, \quad \mathcal{T} = \nabla \mathcal{H} \end{aligned} \quad (14)$$

Eq.14 is the final form of TV-TRPCA optimization problem.

Algorithm 1: TV-TRPCA optimization method

Input: 1.Observation tensor \mathcal{O} .

2.Equilibrium factors $\lambda_1, \lambda_2, \lambda_3, \lambda_4$.

3.Penalty scalars $\mu_0, \nu_0, \mu_{max}, \nu_{max}$, ratio ρ .

4.Variation weights $\sigma_m, \sigma_n, \sigma_t$.

5.Stopping criteria ϵ .

6.Maximum iteration $imax$.

Output: 1.Foreground layer \mathcal{H} .

2.Background layer \mathcal{B} .

3.Dynamic background layer \mathcal{E} .

4.Gaussian noise layer \mathcal{G} .

Initialization:

$\mathcal{B}_0 = \mathcal{R}_0 = \mathcal{G}_0 = \mathcal{E}_0 = \mathcal{H}_0 = \mathcal{X}_0 = \mathcal{Y}_0 = \mathbb{O}^{M \times N \times T}$. $\mathcal{T}_0 = \mathcal{Z}_0 = \mathbb{O}^{M \times N \times 3T}$. $k = 0$.

```
1 while not converged and  $k < imax$  do
2   Update  $\mathcal{B}_{k+1}$  via Eq.19;
3   Update  $\mathcal{R}_{k+1}$  via Eq.20;
4   Update  $\mathcal{G}_{k+1}$  via Eq.21;
5   Update  $\mathcal{E}_{k+1}$  via Eq.22;
6   Update  $\mathcal{H}_{k+1}$  via Eq.30;
7   Update  $\mathcal{T}_{k+1}$  via Eq.32;
8   Update  $\mathcal{X}_{k+1}, \mathcal{Y}_{k+1}, \mathcal{Z}_{k+1}, \mu_{k+1}, \nu_{k+1}$  via Eq.33;
9    $k = k + 1$ .
10  Check the convergence condition:
11   $\|\mathcal{O} - \mathcal{B}_{k+1} - \mathcal{G}_{k+1} - \mathcal{E}_{k+1} - \mathcal{H}_{k+1}\|_F^2 \leq \epsilon \|\mathcal{O}\|_F^2$ 
12 end while
13 return  $\mathcal{B}, \mathcal{G}, \mathcal{E}, \mathcal{H}$ 
```

2.1.6. Optimization Strategy

For the convex optimization problem of matrix recovery, the common solving methods include accelerated proximal gradient (APG), dual approach (DA), iterative thresholding (IT), augmented Lagrange multipliers (ALM) and alternating direction method of multipliers (ADMM) algorithms[68, 69, 70].

Since ADMM strategy has low solving complexity and can guarantee the convergence in most cases, we adopt ADMM based on ALM to solve the optimization problem of Eq.14.

The augmented Lagrange function of Eq.14 is given by:

$$\begin{aligned}
\mathcal{L}(\mathcal{B}, \mathcal{R}, \mathcal{G}, \mathcal{E}, \mathcal{H}, \mathcal{T}; \mu, \nu) = & \\
& \|\mathcal{B}\|_{\otimes} + \lambda_1 \|\mathcal{R}\|_1 + \frac{\lambda_2}{2} \|\mathcal{G}\|_F^2 + \lambda_3 \|\mathcal{E}\|_1 + \lambda_4 \|\mathcal{T}\|_1 \\
& + \frac{\mu}{2} \|\mathcal{O} - \mathcal{B} - \mathcal{R} - \mathcal{G}\|_F^2 + \langle \mathcal{X}, \mathcal{O} - \mathcal{B} - \mathcal{R} - \mathcal{G} \rangle \\
& + \frac{\mu}{2} \|\mathcal{R} - \mathcal{E} - \mathcal{H}\|_F^2 + \langle \mathcal{Y}, \mathcal{R} - \mathcal{E} - \mathcal{H} \rangle \\
& + \frac{\nu}{2} \|\mathcal{T} - \nabla \mathcal{H}\|_F^2 + \langle \mathcal{Z}, \mathcal{T} - \nabla \mathcal{H} \rangle
\end{aligned} \tag{15}$$

where $\mathcal{X}, \mathcal{Y} \in \mathbb{R}^{M \times N \times T}$ and $\mathcal{Z} \in \mathbb{R}^{M \times N \times 3T}$ are the Lagrangian multiplier tensors, μ and ν are positive penalty scalars. Because of the huge number of variables in the augmented Lagrange function, it is difficult to optimize them simultaneously. With the ADMM strategy, we optimize one variable at a time and constrain the other variables to remain constant, alternating until the convergence condition is satisfied. At the end of each iteration, the values of μ and ν will increase, making objective function more sensitive to the change of variables. Specifically, we can decompose the minimization problem of Eq.15 into six sub-problems:

① \mathcal{B} sub-problem:

In the $(k + 1)^{th}$ iteration, for the \mathcal{B} sub-problem optimization, the objective function is:

$$\begin{aligned}
\mathcal{B}_{k+1} = \arg \min_{\mathcal{B}} \mathcal{L}(\mathcal{B}, \mathcal{R}_k, \mathcal{G}_k, \mathcal{E}_k, \mathcal{H}_k, \mathcal{T}_k, \mu_k, \nu_k) & \\
= \arg \min_{\mathcal{B}} \|\mathcal{B}\|_{\otimes} + \frac{\mu_k}{2} \|\mathcal{O} - \mathcal{B} - \mathcal{R}_k - \mathcal{G}_k\|_F^2 & \\
+ \langle \mathcal{X}_k, \mathcal{O} - \mathcal{B} - \mathcal{R}_k - \mathcal{G}_k \rangle & \\
= \arg \min_{\mathcal{B}} \|\mathcal{B}\|_{\otimes} + \frac{\mu_k}{2} \|\mathcal{O} - \mathcal{B} - \mathcal{R}_k - \mathcal{G}_k + \frac{\mathcal{X}_k}{2}\|_F^2 & \\
= \arg \min_{\mathcal{B}} \|\mathcal{B}\|_{\otimes} + \frac{\mu_k}{2} \|\mathcal{A} - \mathcal{B}\|_F^2 &
\end{aligned} \tag{16}$$

where $\mathcal{A} = \mathcal{O} - \mathcal{R}_k - \mathcal{G}_k + \mathcal{X}_k/2$. In [13], TNN was proved to have a closed-form solution as the proximal operator of the matrix nuclear norm. In this case, suppose $\mathcal{A} = \mathcal{U} * \mathcal{S} * \mathcal{V}^*$ is the t-SVD of $\mathcal{A} \in \mathbb{R}^{M \times N \times T}$, the tensor Singular Value Thresholding (t-SVT) operator is defined as

$$\mathcal{D}_{\mu_k}(\mathcal{A}) = \mathcal{U} * \mathcal{S}_{\mu_k^{-1}} * \mathcal{V}^* \tag{17}$$

where

$$\mathcal{S}_{\mu_k^{-1}} = \mathbf{ifft} \left(\max(\tilde{\mathcal{S}} - \mu_k^{-1}, 0), [1, 3] \right) \tag{18}$$

The t-SVT operator $\mathcal{D}_{\mu_k}(\mathcal{A})$ simply applies a soft-thresholding rule to the singular values $\tilde{\mathcal{S}}$ of the frontal slices of $\tilde{\mathcal{A}}$, effectively shrinking these towards zero[13]. Finally, the \mathcal{B} sub-problem optimization can be computed by

$$\mathcal{B}_{k+1} = \mathcal{D}_{\mu_k} \left(\mathcal{O} - \mathcal{R}_k - \mathcal{G}_k + \frac{\mathcal{X}_k}{2} \right) \tag{19}$$

② \mathcal{R} sub-problem:

In the $(k + 1)^{th}$ iteration, for the \mathcal{R} sub-problem optimization, the objective function is:

$$\begin{aligned}
\mathcal{R}_{k+1} &= \arg \min_{\mathcal{R}} \mathcal{L}(\mathcal{B}_{k+1}, \mathcal{R}, \mathcal{G}_k, \mathcal{E}_k, \mathcal{H}_k, \mathcal{T}_k, \mu_k, \nu_k) \\
&= \arg \min_{\mathcal{R}} \lambda_1 \|\mathcal{R}\|_1 + \frac{\mu_k}{2} \|\mathcal{O} - \mathcal{B}_{k+1} - \mathcal{R} - \mathcal{G}_k\|_F^2 \\
&\quad + \langle \mathcal{X}_k, \mathcal{O} - \mathcal{B}_{k+1} - \mathcal{R} - \mathcal{G}_k \rangle \\
&\quad + \frac{\mu_k}{2} \|\mathcal{R} - \mathcal{E}_k - \mathcal{H}_k\|_F^2 + \langle \mathcal{R} - \mathcal{E}_k - \mathcal{H}_k \rangle \\
&= \arg \min_{\mathcal{R}} \lambda_1 \|\mathcal{R}\|_1 + \mu_k \|\mathcal{Q} - \mathcal{R}\|_F^2 \\
&= \mathcal{S}_{\frac{\lambda_1}{2\mu_k}}(\mathcal{Q})
\end{aligned} \tag{20}$$

where $\mathcal{Q} = (\mathcal{O} - \mathcal{B}_{k+1} - \mathcal{G}_k + \mathcal{E}_k + \mathcal{H}_k)/2 + (\mathcal{X}_k - \mathcal{Y}_k)/2\mu_k$. $\mathcal{S}_a(b) = \text{sgn}(b)\max(|b| - a, 0)$ is the shrinkage operator of a scalar and Eq.20 is the extension to tensor \mathcal{Q} element-wisely.

③ \mathcal{G} sub-problem:

In the $(k + 1)^{th}$ iteration, for the \mathcal{G} sub-problem optimization, the objective function is:

$$\begin{aligned}
\mathcal{G}_{k+1} &= \arg \min_{\mathcal{G}} \mathcal{L}(\mathcal{B}_{k+1}, \mathcal{R}_{k+1}, \mathcal{G}, \mathcal{E}_k, \mathcal{H}_k, \mathcal{T}_k, \mu_k, \nu_k) \\
&= \arg \min_{\mathcal{G}} \frac{\lambda_2}{2} \|\mathcal{G}\|_F^2 + \frac{\mu_k}{2} \|\mathcal{O} - \mathcal{B}_{k+1} - \mathcal{R}_{k+1} - \mathcal{G}\|_F^2 \\
&\quad + \langle \mathcal{X}_k, \mathcal{O} - \mathcal{B}_{k+1} - \mathcal{R}_{k+1} - \mathcal{G} \rangle \\
&= \frac{\mu_k}{\lambda_2 + \mu_k} \left(\mathcal{O} - \mathcal{B}_{k+1} - \mathcal{R}_{k+1} + \frac{\mathcal{X}_k}{\mu_k} \right)
\end{aligned} \tag{21}$$

④ \mathcal{E} sub-problem:

In the $(k + 1)^{th}$ iteration, for the \mathcal{E} sub-problem optimization, the objective function is:

$$\begin{aligned}
\mathcal{E}_{k+1} &= \arg \min_{\mathcal{E}} \mathcal{L}(\mathcal{B}_{k+1}, \mathcal{R}_{k+1}, \mathcal{G}_{k+1}, \mathcal{E}, \mathcal{H}_k, \mathcal{T}_k, \mu_k, \nu_k) \\
&= \arg \min_{\mathcal{E}} \lambda_3 \|\mathcal{E}\|_1 + \frac{\mu_k}{2} \|\mathcal{R}_{k+1} - \mathcal{E} - \mathcal{H}_k\|_F^2 \\
&\quad + \langle \mathcal{Y}_k, \mathcal{R}_{k+1} - \mathcal{E} - \mathcal{H}_k \rangle \\
&= \arg \min_{\mathcal{E}} \lambda_3 \|\mathcal{E}\|_1 + \frac{\mu_k}{2} \|\mathcal{P} - \mathcal{E}\|_F^2 \\
&= \mathcal{S}_{\frac{\lambda_3}{\mu_k}}(\mathcal{P})
\end{aligned} \tag{22}$$

where $\mathcal{P} = \mathcal{R}_{k+1} - \mathcal{H}_k + \mathcal{Y}_k/\mu_k$. The solution of \mathcal{E} sub-problem is similar to \mathcal{R} sub-problem.

⑤ \mathcal{H} sub-problem: In the $(k + 1)^{th}$ iteration, for the \mathcal{H} sub-problem optimization, the objective function is:

$$\begin{aligned}
\mathcal{H}_{k+1} &= \arg \min_{\mathcal{H}} \mathcal{L}(\mathcal{B}_{k+1}, \mathcal{R}_{k+1}, \mathcal{G}_{k+1}, \mathcal{E}_{k+1}, \mathcal{H}, \mathcal{T}_k, \mu_k, \nu_k) \\
&= \arg \min_{\mathcal{H}} \frac{\mu_k}{2} \|\mathcal{R}_{k+1} - \mathcal{E}_{k+1} - \mathcal{H}\|_F^2 \\
&\quad + \langle \mathcal{Y}_k, \mathcal{R}_{k+1} - \mathcal{E}_{k+1} - \mathcal{H} \rangle + \frac{\nu_k}{2} \|\mathcal{T}_k - \nabla \mathcal{H}\|_F^2 \\
&\quad + \langle \mathcal{Z}_k, \mathcal{T}_k - \nabla \mathcal{H} \rangle
\end{aligned} \tag{23}$$

Since there are tensors of different sizes in Eq.23, for the sake of convenience, we use tensor vectorization to simplify the computation. Define operator $\mathbf{Vec}(\mathcal{X}) = f(\mathcal{X}) \in \mathbb{R}^{MNT}$ transforms the 3-D tensor $\mathcal{X} \in \mathbb{R}^{M \times N \times T}$ to a 1-D vector and $f^{-1}(\mathcal{X})$ is the inverse operator, the variances of \mathcal{X} in each dimension can be vectorized into the product of a block circulant matrix and the tensor vectorization $f(\mathcal{X})$, i.e.,

$$f(\nabla_i \mathcal{H}) = \mathbf{D}_i f(\mathcal{H}), \quad i = m, n, t \tag{24}$$

where $\mathbf{D}_m, \mathbf{D}_n, \mathbf{D}_t \in \mathbb{R}^{MNT \times MNT}$ are block circulant matrices. Let $\mathbf{D} = [\sigma_m \mathbf{D}_m^T, \sigma_n \mathbf{D}_n^T, \sigma_t \mathbf{D}_t^T]^T \in \mathbb{R}^{3MNT \times MNT}$, according to Eq.10, we have

$$f(\nabla \mathcal{H}) = \mathbf{D} f(\mathcal{H}) \tag{25}$$

Now we can rewrite Eq.23 as follows (the derivation use the property that the transpose of a scalar is itself):

$$\begin{aligned}
\mathcal{H}_{k+1} &= \arg \min_{\mathcal{H}} \frac{\mu_k}{2} \|\mathcal{R}_{k+1} - \mathcal{E}_{k+1} - \mathcal{H}\|_F^2 \\
&\quad + \langle \mathcal{Y}_k, \mathcal{R}_{k+1} - \mathcal{E}_{k+1} - \mathcal{H} \rangle + \frac{\nu_k}{2} \|f(\mathcal{T}_k) - \mathbf{D} f(\mathcal{H})\|_F^2 \\
&\quad + \langle f(\mathcal{Z}_k), f(\mathcal{T}_k) - \mathbf{D} f(\mathcal{H}) \rangle \\
&= \arg \min_{\mathcal{H}} \frac{1}{2} \left(\mu_k f^T(\mathcal{H}) f(\mathcal{H}) + \nu_k f^T(\mathcal{H}) \mathbf{D}^T \mathbf{D} f(\mathcal{H}) \right) \\
&\quad - \mu_k f^T(\mathcal{H}) f \left(\mathcal{R}_{k+1} - \mathcal{E}_{k+1} + \frac{\mathcal{Y}_k}{\mu_k} \right) \\
&\quad - \nu_k f^T(\mathcal{H}) \mathbf{D}^T f \left(\mathcal{T}_k + \frac{\mathcal{Z}_k}{\nu_k} \right) \\
&= \arg \min_{\mathcal{H}} \phi(f(\mathcal{H}))
\end{aligned} \tag{26}$$

Notice that

$$\mathbf{D}^T \mathbf{D} = \sigma_m^2 \mathbf{D}_m^T \mathbf{D}_m + \sigma_n^2 \mathbf{D}_n^T \mathbf{D}_n + \sigma_t^2 \mathbf{D}_t^T \mathbf{D}_t \tag{27}$$

is positive definite, so Eq.26 can be solved by the normal equation of convex function $\phi(f(\mathcal{H}))$.

Let $\partial \phi(f(\mathcal{H})) / \partial f(\mathcal{H}) = 0$, we can get

$$(\mu_k \mathbf{I} + \nu_k \mathbf{D}^T \mathbf{D}) f(\mathcal{H}_{k+1}) = f(\mathcal{K}) \tag{28}$$

where

$$\mathcal{K} = \mu_k \left(\mathcal{R}_{k+1} - \mathcal{E}_{k+1} + \frac{\mathcal{Y}_k}{\mu_k} \right) + \nu_k f^{-1} \left(\mathbf{D}^T f \left(\mathcal{T}_k + \frac{\mathcal{Z}_k}{\nu_k} \right) \right) \quad (29)$$

\mathcal{H}_{k+1} can be directly solved by computing the Moore-Penrose pseudoinverse of matrix $\mu_k \mathbf{I} + \nu_k \mathbf{D}^T \mathbf{D}$, but this will occupy huge memory space, resulting in low computational efficiency. Consider that the block circulant matrix can be diagonalized by the DFT matrix[71, 72], hence Eq.28 has the following solution (See Appendix A for the details)

$$\mathcal{H}_{k+1} = f^{-1} \left(\mathbf{ifft} \left(\frac{\mathbf{fft}(f(\mathcal{K}))}{\mathbf{diagv}(\mu_k \mathbf{I} + \nu_k \mathbf{K})} \right) \right) \quad (30)$$

where

$$\mathbf{K} = \sigma_m^2 |\mathbf{fft}(\mathbf{D}_m)|^2 + \sigma_n^2 |\mathbf{fft}(\mathbf{D}_n)|^2 + \sigma_t^2 |\mathbf{fft}(\mathbf{D}_t)|^2 \quad (31)$$

where $\mathbf{diagv}(\cdot)$ forms a column vector from the elements of the diagonal of a matrix, $|\cdot|^2$ is the element-wise square, and the division is also performed element-wisely. The denominator in Eq.30 can be precalculated outside the iteration, reducing the computational complexity.

⑥ \mathcal{T} sub-problem:

In the $(k+1)^{th}$ iteration, for the \mathcal{T} sub-problem optimization, the objective function is:

$$\begin{aligned} \mathcal{T}_{k+1} &= \arg \min_{\mathcal{T}} \mathcal{L}(\mathcal{B}_{k+1}, \mathcal{R}_{k+1}, \mathcal{G}_{k+1}, \mathcal{E}_{k+1}, \mathcal{H}_{k+1}, \mathcal{T}, \mu_k, \nu_k) \\ &= \arg \min_{\mathcal{T}} \lambda_4 \|\mathcal{T}\|_1 + \frac{\nu_k}{2} \|\mathcal{T} - \nabla \mathcal{H}_{k+1}\|_F^2 \\ &\quad + \langle \mathcal{Z}_k, \mathcal{T} - \nabla \mathcal{H}_{k+1} \rangle \\ &= \arg \min_{\mathcal{E}} \lambda_4 \|\mathcal{T}\|_1 + \frac{\nu_k}{2} \|\mathcal{T} - \nabla \mathcal{H}_{k+1} + \frac{\mathcal{Z}_k}{\nu_k}\|_F^2 \\ &= \mathcal{S}_{\frac{\lambda_4}{\nu_k}}(\mathcal{W}) \end{aligned} \quad (32)$$

where $\mathcal{W} = \nabla \mathcal{H}_{k+1} - \mathcal{Z}_k / \nu_k$. The solution of \mathcal{T} sub-problem is similar to \mathcal{R} and \mathcal{E} sub-problem.

After solving all the six sub-problems, the Lagrangian multipliers and penalty scalars are updated by

$$\begin{cases} \mathcal{X}_{k+1} = \mathcal{X}_k + \mu_k (\mathcal{O} - \mathcal{B}_{k+1} - \mathcal{R}_{k+1} - \mathcal{G}_{k+1}) \\ \mathcal{Y}_{k+1} = \mathcal{Y}_k + \mu_k (\mathcal{R}_{k+1} - \mathcal{E}_{k+1} - \mathcal{H}_{k+1}) \\ \mathcal{Z}_{k+1} = \mathcal{Z}_k + \nu_k (\mathcal{T}_{k+1} - \nabla \mathcal{H}_{k+1}) \\ \mu_{k+1} = \min(\rho \mu_k, \mu_{max}) \\ \nu_{k+1} = \min(\rho \nu_k, \nu_{max}) \end{cases} \quad (33)$$

where ρ is the increase ratio of penalty scalars μ and ν .

The entire algorithm of optimizing Eq.14 has been summarized in Algorithm 1. The iteration terminates when the convergence condition is satisfied, or the maximal number of iteration is reached.

We use TV-TRPCA method to process an XCA image sequence and show the results of foreground extraction for different frames in Fig.2. In frame 9, the contrast agent was just been injected. In frame 14-37, the contrast agent

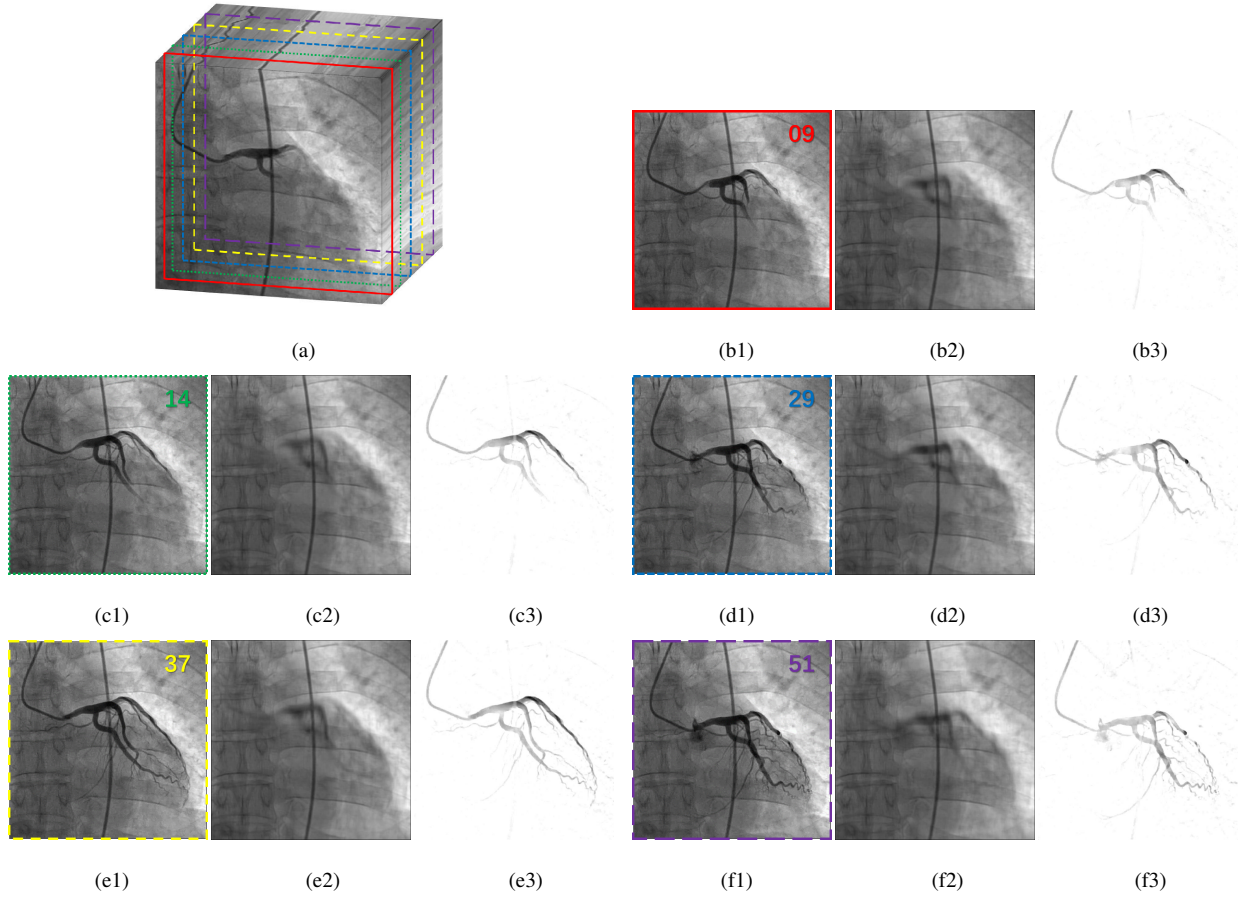


Figure 2: TV-TRPCA foreground extraction. (a) is the 3D-tensor formed by XCA image sequence and its 9^{th} , 14^{th} , 29^{th} , 37^{th} , 51^{th} frontal slices. (b1)-(f1) is the original image, (b2)-(f2) are the background layers, (b3)-(f3) are the vessel foreground layers. In order to improve the visibility of vessel layers, gray scale normalization is adopted.

gradually diffused completely. In frame 51, the contrast agent began to dissipate. In order to facilitate observation, we normalized the gray scale of the foreground layer. It can be found that the vessel layer is well separated during the whole process, and the dynamic background and high-frequency noise are well suppressed. The static background also retains high low-rank property.

2.2. Vessel Segmentation

The vessel layer extracted by TV-TRPCA could have uneven gray distribution and local fracture, affecting the accuracy of subsequent quantitative analysis. The method of vessel segmentation can effectively solve these two problems.

2.2.1. Region Growing

Region growing is a model-based image segmentation method. Based on the similarity of gray values, region growing method combines pixels in digital images according to certain rules to form regions of interest[73, 74].

Therefore, this method mainly needs to determine the seed point of growing, the region growing criterion and the termination condition of stopping growing.

In this paper, seed point is automatically selected based on the maximum criterion of local gray intensity[7]. To be specific, a disk with its diameter close to aorta is used to match the extracted vessel layer image. When all points in the disk have the densest gray scale, the center of the disk is the initial seed point of region growing, which can effectively avoid the interference caused by residual noise. According to the gray threshold, the points in its four neighborhood are classified and the next seed point is selected until there is no pixel point that meets the growing criterion.

2.2.2. RLF filter

The region growing method can extract continuous vessel branches extending from the aorta, but broken segments will be deleted. Consider the unique ridge structure of the microvessel segment, we adopt the Radon-like features (RLF) filter[18] to enhance the extracted vessel layer image. It uses edge sensing in different directions to make non-isotropic sampling of the neighborhood, which can highlight and extend the tubular structures.

Before extracting radon features of coronary artery, the image was first convolved by an edge enhancing Gaussian second derivative (GSD) filter as follows[18]

$$\mathbf{G}(x, y) = \max_{\sigma, \theta} \Delta \mathbf{G}(\sigma, \theta) \otimes \mathbf{I}(x, y) \quad (34)$$

where σ and θ are the scale and direction of GSD filter, \otimes is the convolution operator, \mathbf{I} is the original image.

The nodes of Radon-like features are defined by the edge graph of image $\mathbf{G}(x, y)$ while the extraction function is defined as a mean function between two nodes, i.e.,[18]

$$T(\mathbf{I}, \mathbf{l}(t)) = \frac{\int_{t_i}^{t_{i+1}} \mathbf{G}(\mathbf{l}(t)) \delta t}{\|\mathbf{l}(t_{i+1}) - \mathbf{l}(t_i)\|_2}, \quad t \in [t_i, t_{i+1}] \quad (35)$$

where \mathbf{l} is the scanning line along which features are enhanced, t is the nodes set where \mathbf{l} intersects the edge graph. Changing the slope and intercept of \mathbf{l} , different images with the same size of \mathbf{I} can be obtained by combine the extraction function value of each pixel. Averaging the gray values of these images gives the final RLF filtering result \mathbf{R} .

2.2.3. Two-stage Region Growing

Although RLF filtering enhance and connect the microvessel segments. As shown in Fig.3, for thick vessels such as the aorta, it only enhances the edge information, producing internal voids. So RLF filtering is not suitable for global vessel segmentation. Based on the previous analysis, a two-stage regional growing vessel segmentation method is presented in this section. The sections in the blue box in Fig.3 gives a more intuitive representation of the details.

In the first stage, a global threshold segmentation is used as the preprocessing to delete the residual low gray level noise. Since most of the noise has been removed after foreground extraction, we use 95% of the maximum gray value as the threshold for binarization. Compared with other complex threshold segmentation algorithms[20, 21],

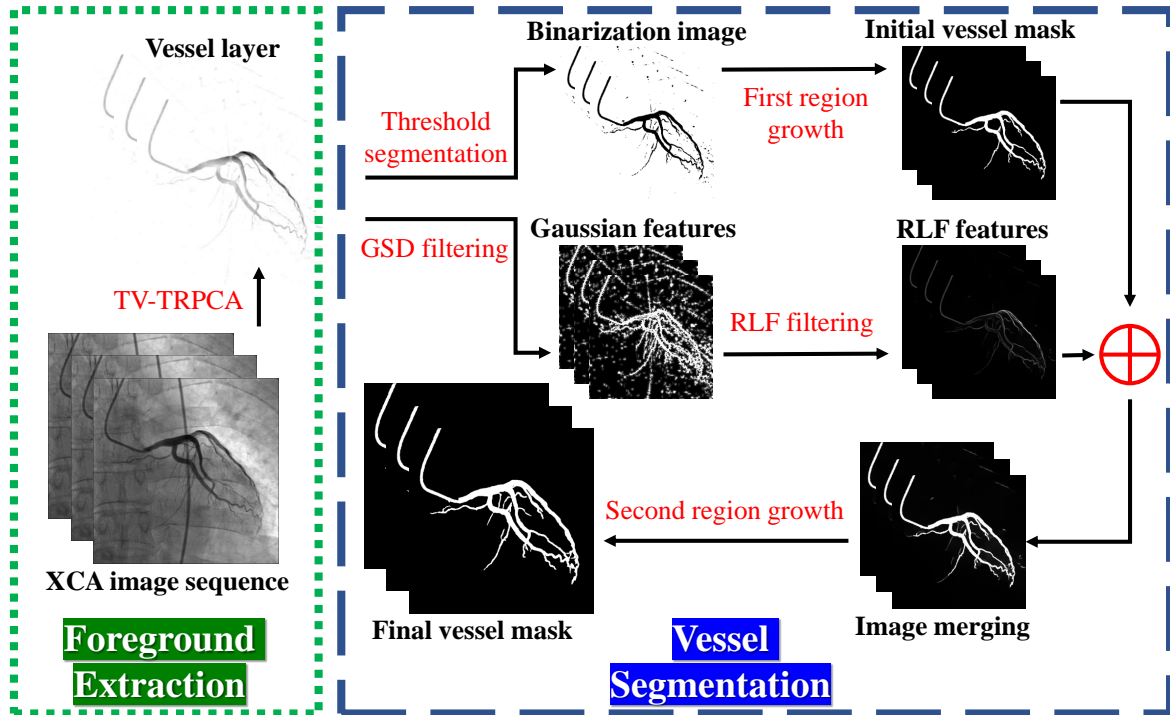


Figure 3: The whole process of proposed method, including TV-TRPCA vessel foreground extraction and TSRG vessel segmentation.

this procedure can preserve more vessel information in low-noise images. The vessel mask of main branches can be obtained by performing region growing on the binary image.

In the second stage, the RLF filtering is utilized on the original vessel layer image to get a edge-like graph. Superimposing (Summing their gray scale values) this edge-like graph on the vessel mask obtained in the first stage gives an image with more detailed features. The second region growing is performed on this image to obtain the final vessel mask.

2.3. Overview of the Whole Process

The whole process of our method is shown in Fig.3 We first use TV-TRPCA optimization method to extract the vessel foreground layer, then perform a TSRG algorithm for vessel segmentation. Finally, a complete tubular coronary mask was obtained.

3. Experimental Results

3.1. Original XCA Data and Gold Standard

We first took 7 real clinical XCA image sequences as the original experimental data for the evaluation of proposed TV-TRPCA and TSRG methods. All these sequences were obtained from Ruijin Hospital affiliated to Shanghai Jiao

Ground Truth AccAltProj MoG-RPCA MCR-RPCA ETRPCA KBR-RPCA TNN-TRPCA TV-TRPCA

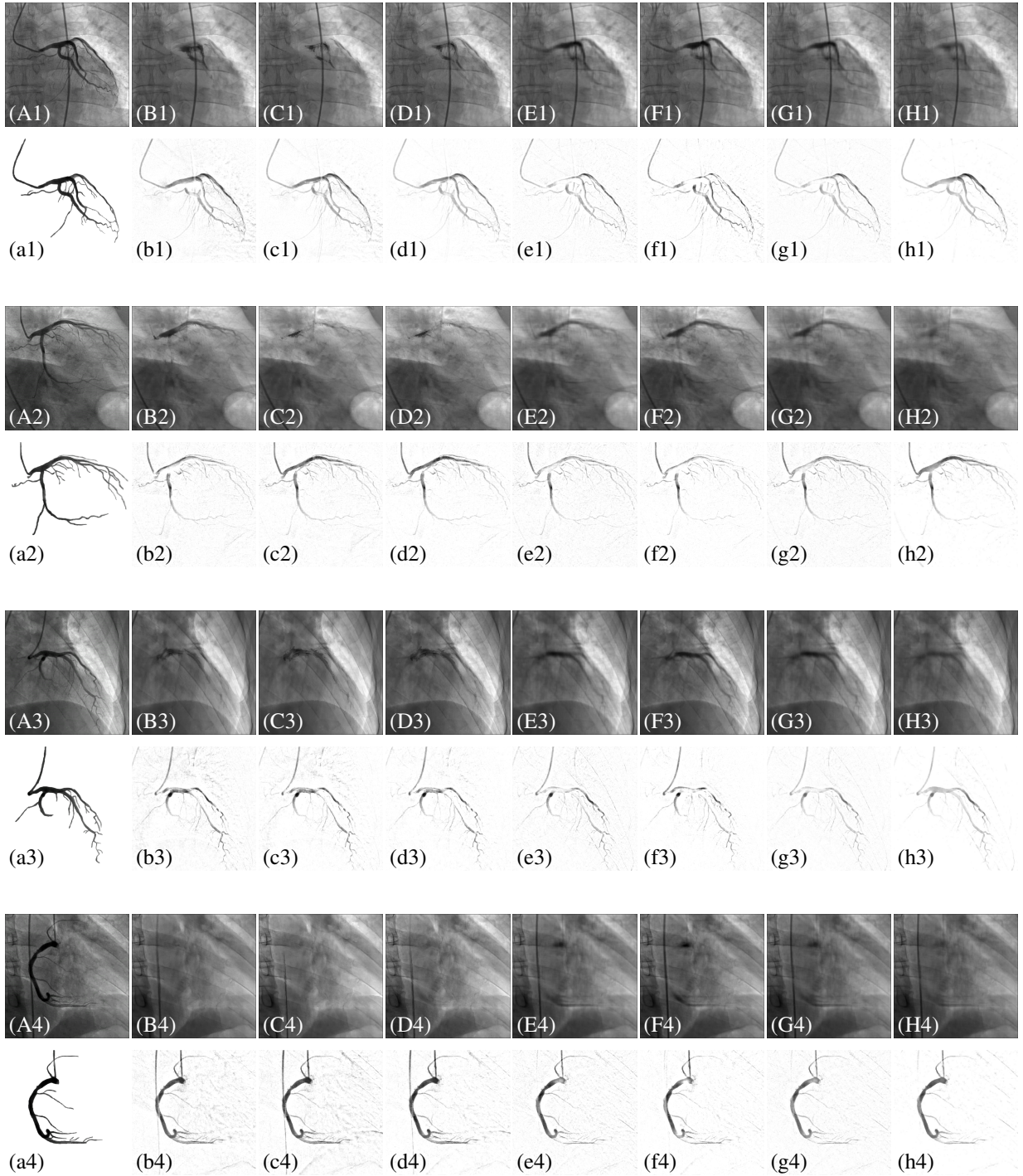


Figure 4: Foreground extraction results of 4 XCA image sequences by 7 layer separation approaches. Each group of results contains a background layer image labeled by capital letters (B-H) and a vessel foreground layer image labeled by lowercase letters (b-h). (A1)-(A4) and (a1)-(a4) are the original XCA images and their ground truth vessel masks selected by the surgeon. (B,b) AccAltProj. (C,c) MoG-RPCA. (D,d) MCR-RPCA. (E,e) ETRPCA. (F,f) KBR-RPCA. (G,g) TNN-TRPCA. (H,h) TV-TRPCA.

Tong University, including left coronary artery (LCA) and right coronary artery (RCA) angiograms in different positions such as AP, LAO/RAO and CRAN/CAUD. Each sequence is consisted of 60 continuous frames with resolution of 656×656 pixels and 8 bits per pixel. Furthermore, to exam the stability and applicability of our methods, we did the same experiment with the database of TÜRKER TUNCER updated on *Kaggle*². This database contains 51 groups of XCA image sequences in four different positions, and each sequence is consisted of 10 continuous frames with resolution of 512×512 pixels and 8 bits per pixel. In the experiment, we randomly selected 10 sequences from the database for calculation.

For quantitative analysis, experienced surgeons were invited to precisely segment the original XCA images and the ground truth (GT) vessel masks were obtained, as shown in Fig.4. (a1)-(a4), which are used as the gold standard of the foreground layer. Due to the blurred vessel edge, the artificially selected vessel foreground area will be widened. In the experiment of vessel segmentation, the GT vessel mask is processed with smooth edge contraction to make the binary vessel mask more accurate, as shown in Fig.7. (a1)-(a4).

3.2. Experiment Design

The main Experiment is divided into two parts: foreground extraction and vessel segmentation. In the TV-TRPCA algorithm, the parameter is set to $\lambda_1 = 0.3/\sqrt{\max(M,N) \times T}$, $\lambda_2 = 100\lambda_1$, $\lambda_3 = 2.5\lambda_1$, $\lambda_4 = 0.6\lambda_1$, $\mu_0 = \nu_0 = 1e^{-4}$, $\mu_{max} = \nu_{max} = 1e^{10}$, $\rho = 1.1$, $\sigma_m = \sigma_n = \sigma_t = 1$, $\epsilon = 1e^{-4}$, $imax = 100$. In the TSRG algorithm, the codes of RLF filtering are form the third-party libraries of MATLAB³, the parameters are adjusted to $sup = 25$, $or = 1$, $sc = 10$. And four-neighborhood sampling is used in region growing. For comparison, we investigated some open-source state-of-the-art approaches and tested their performance.

In foreground extraction part, three RPCA methods *AccAltProj*⁴[75], *MoG-RPCA*⁵[67], *MCR-RPCA*⁶[64] and three TRPCA methods *ETRPCA*⁷[57], *KBR-RPCA*⁸[53], *TNN-TRPCA*⁹[13] were introduced as the control groups. To make it more adaptive to XCA vessel layer extraction, we optimized the parameters of these six algorithms in detail.

In vessel segmentation part, traditional Hessian based multi-scale Frangi filtering¹⁰[15], DSA[32], moving objects detection method *DECOLOR*¹¹[76] and U-net based vessel segmentation method¹²[31] were introduced as the control groups. All the parameters in these four algorithms are also optimized to get better segmentation results.

²<https://www.kaggle.com/datasets/turkertuncer/coronary-angiography-print>

³<https://ww2.mathworks.cn/matlabcentral/fileexchange/27886-radon-like-features>

⁴https://github.com/caesarcai/AccAltProj_for_RPCA

⁵<https://github.com/timmyzhao/MoG-RPCA>

⁶<https://github.com/Binjie-Qin/MCR-RPCA>

⁷https://github.com/xdweixia/TPAMI2020_ETRPCA

⁸<https://github.com/XieQi2015/KBR-TC-and-RPCA>

⁹<https://github.com/canyilu/Tensor-Robust-Principal-Component-Analysis-TRPCA>

¹⁰<https://ww2.mathworks.cn/matlabcentral/fileexchange/24409-hessian-based-frangi-vesselness-filter>

¹¹<https://fling.seas.upenn.edu/xiaowz/dynamic/wordpress/decolor>

¹²<https://github.com/thanosvlo/Deep-Segmentation-and-Registration-in-X-Ray-Angiography-Video>

All the experiments were programmed in Matlab R2020a, ran on a low cost personal laptop with an Intel (R) Core (TM) i7-11700H 3.2GHz CPU and 16GB 3200MHz Memory.

3.3. Foreground Extraction Visibility Evaluation

The vessel foreground extraction results of proposed TV-TRPCA method and 6 comparison methods are shown in Fig.4. Three RPCA-based methods AccAltProj, MoG-RPCA and MCR-RPCA show better continuity of foreground vessel layer at the expense of smoothness of background layer. It can be seen that the background gray scale obtained by these three methods is extremely uneven, with a large number of tubular artifacts. This is because the high-dimensional spatial-temporal information is destroyed and reorganized in the operation of matricize. As a comparison, three TRPCA-based methods ETRPCA, KBR-RPCA and TNN-TRPCA perform well in the gray uniformity of background layer. However, for the aorta moving slowly in the foreground, these three methods all classified it as the background part, resulting in the cavitation of the foreground vessel layer. Due to the high-order information recovery ability of TRPCA and the constraint of TV on the foreground, the proposed method TV-TRPCA performs better in both the low-rank property of background and the continuity of foreground, and the dynamic noise in the foreground vessel layer is also well suppressed.

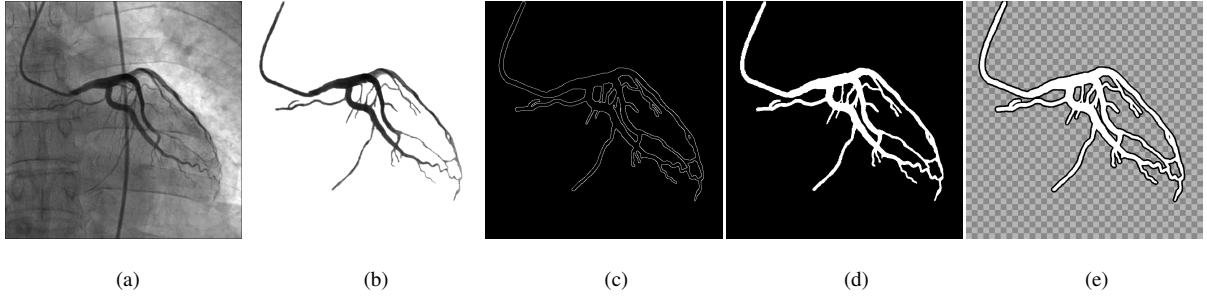


Figure 5: Global CNR and Local CNR. (a) is the original XCA image. (b) is the Ground truth vessel mask. (c) is the edge of vessel region. (d) is the demonstration of Global CNR. (e) is the demonstration of Local CNR. The evenly distributed squares represent transparent regions that are not included in the calculation.

In order to quantitatively evaluate and compare the visibility of the extracted foreground by each method, the contrast-to-noise ratio (CNR)[44] is introduced and defined as

$$CNR = \frac{|\mu_v - \mu_b|}{\sigma_b} \quad (36)$$

where μ_v and μ_b are the mean gray values of vessel region(white area of Fig.5. (d) (e)) and background region(black area of Fig.5. (d) (e)) in foreground layer, σ_b is the standard deviation of background region gray values. CNR reflects the gray value difference between vessel region and background region in foreground layer, the higher the CNR value, the higher the contrast of foreground layer and the better the visibility of vessel region.

Consider that there are a lot of artifacts along the edges of the vessels in foreground layer, to evaluate the global and local visibility respectively, we use two criteria to divide the background area. The first covers all the non-vessel

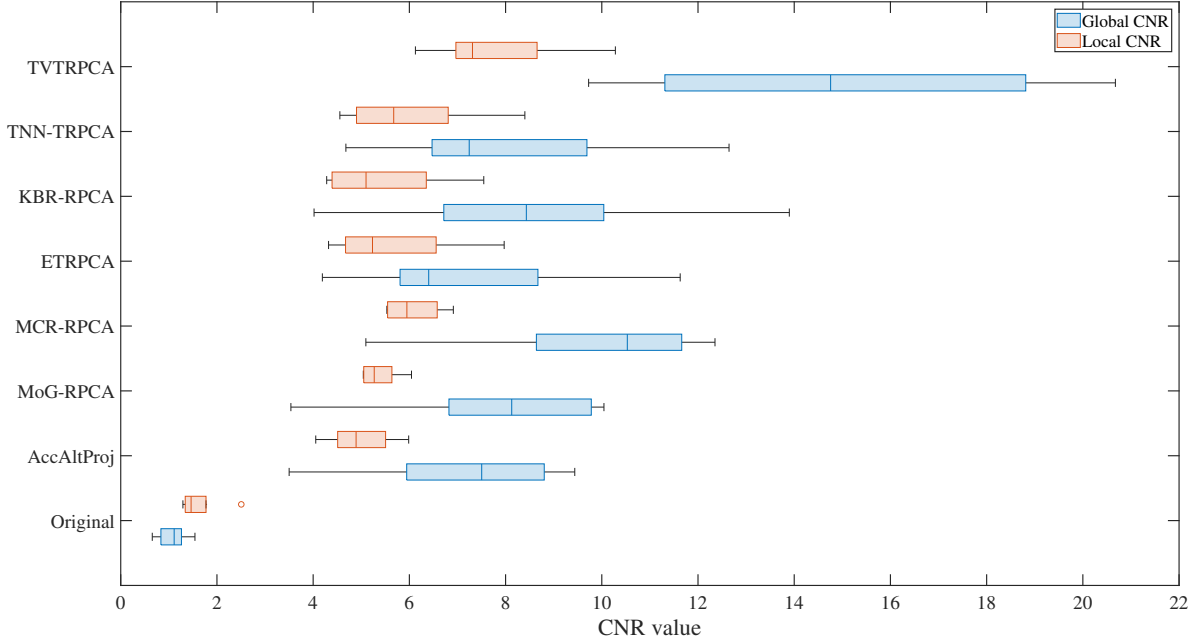


Figure 6: Global CNR and Local CNR values of original XCA image and vessel foreground extracted by different layer separation methods for clinical data.

Table 2: The mean cnr values (\pm standard deviation) and average time costs of different layer separation methods

Method	Clinical			Database		
	Global CNR	Local CNR	Time cost	Global CNR	Local CNR	Time cost
Original	1.0745 ± 0.3306	1.6293 ± 0.4986	\	1.2455 ± 0.2567	1.8769 ± 0.3851	\
AccAltProj	7.1588 ± 2.2864	4.9878 ± 0.7266	18.40s	4.4424 ± 1.6890	3.2138 ± 0.7855	2.68s
MoG-RPCA	7.8643 ± 2.5932	5.3825 ± 0.4147	137.59s	5.9600 ± 2.2811	4.4703 ± 0.5729	25.57s
MCR-RPCA	9.8465 ± 2.8211	6.0829 ± 0.6002	1400.73s	7.1907 ± 2.6614	4.9258 ± 1.1722	423.78s
ETRPCA	7.2509 ± 2.7507	5.6802 ± 1.4362	465.24s	6.6477 ± 2.7086	5.4510 ± 1.0119	82.54s
KBR-RPCA	8.5439 ± 3.5379	5.4622 ± 1.3396	747.07s	6.4012 ± 2.5877	5.0789 ± 1.1416	139.68s
TNN-TRPCA	8.0690 ± 2.9373	5.9847 ± 1.5000	325.36s	6.9790 ± 1.8564	5.5218 ± 1.2676	73.70s
TV-TRPCA	15.0382 ± 4.4796	7.8160 ± 1.5496	506.78s	11.8059 ± 3.7615	6.7382 ± 1.3335	95.88s

region of foreground layer, as shown in Fig.5. (d), which is called the Global CNR. The second are the 4-pixel wide neighborhood area surrounding the vessel region, as shown in Fig.5. (e), which is called the Local CNR.

For clinical XCA image sequences and third-party database, we calculated Global CNR and Local CNR of different foreground extraction methods and recorded the time costs in Tab.2. And Fig6 gives an intuitive distribution of CNR values for clinical images. In this experiment, a frame was randomly selected for each image sequence, 7 clinical images and 10 database images were tested.

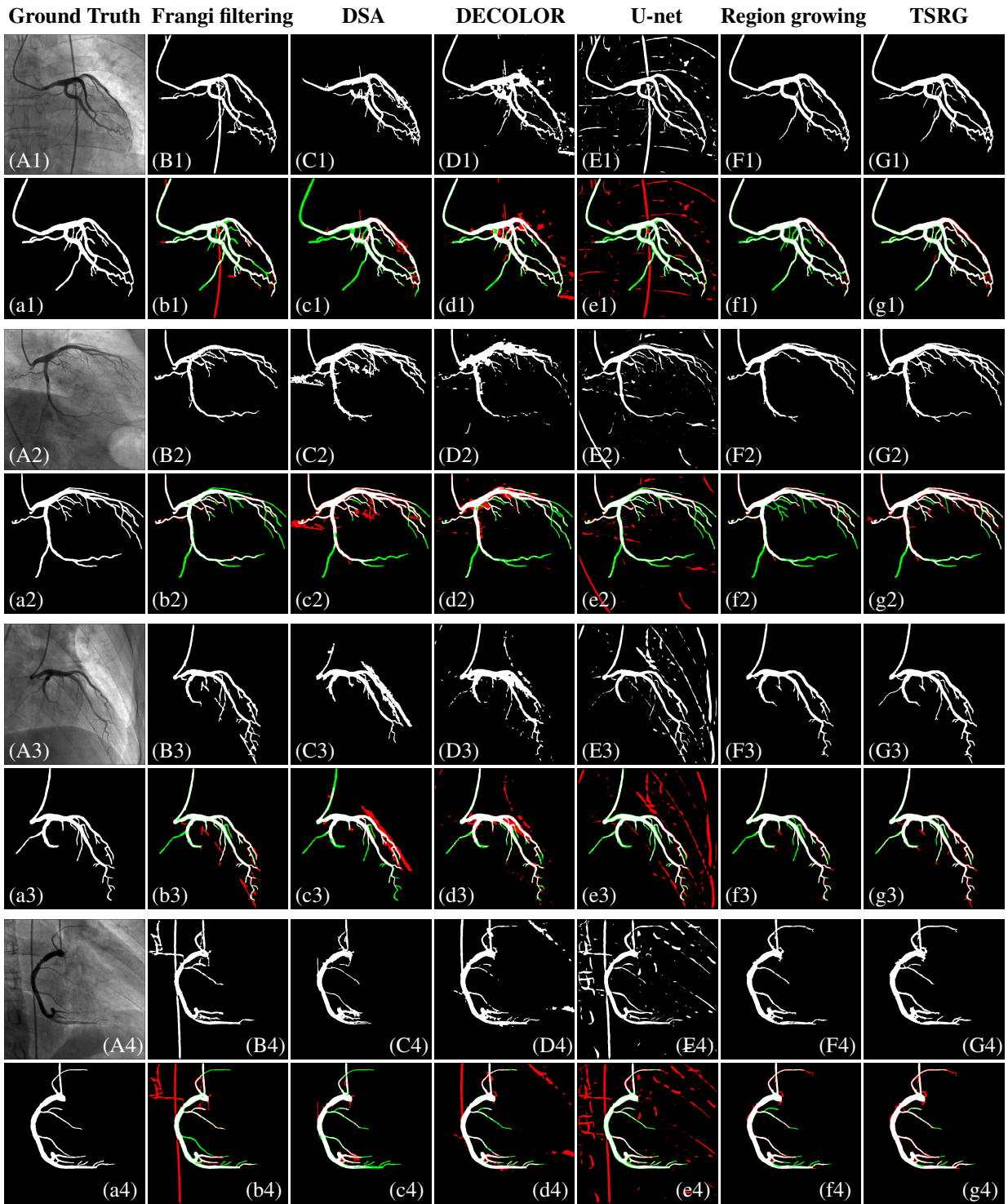


Figure 7: Vessel segmentation results of 4 XCA image sequences by 6 vessel extraction methods. Each group of results contains an initial segmentation image labeled by capital letters (B-H) and its contrast image labeled by lowercase letters (b-h). In (b-h), white area represents the true positive (TP) part, red area represents the false positive (FP) part, green area represents the false negative (FN) part. (A1)-(A4) and (a1)-(a4) are the original XCA images and their ground truth binary vessel masks. (B,b) Frangi filtering. (C,c) DSA. (D,d) DECOLOR. (E,e) U-net. (F,f) First stage region growing. (G,g) TSRG.

3.4. Vessel Segmentation Accuracy Evaluation

The vessel segmentation results of proposed TSRG method and 5 comparison methods are shown in Fig.7. The methods of region growing and TSRG are based on the vessel layer extracted by TV-TRPCA, and the others are based on the original XCA image. For Hessian based multi-scale Frangi filtering and digital subtraction angiography, we performed region growing to transform the intermediate results into binary images. Fig.7. (b-g) compare the segmentation results with the ground truth binary vessel mask and highlight the differences between them. White area represents the true positive (TP) part, red area represents the false positive (FP) part, and green area represents the false negative (FN) part.

For traditional Frangi filtering method, it remains irrelevant tissues, and thick blood vessels are prone to cavities. DSA method can preserve minimal details to the greatest extent, but it amplifies local noise, and the segmentation accuracy is seriously disturbed by vessel movements and contrast agent distribution changes. RPCA-based method DECOLOR and deep neural network U-net can obtain the binary vessel mask directly from the original XCA image, but they can't guarantee the continuity of blood vessels, and there exists a lot of noise in the background. Especially, for U-net method, it identifies all the tubular objects in the original image as segments of blood vessels, which will seriously reduce the segmentation precision (shown in Fig.8). Therefore, it is more suitable for retinal vessel segmentation with less irrelevant tissue and noise. For Region growing and TSRG methods based on vessel layer extracted by TV-TRPCA, the former well segments the continuous vessel area, but vessels outside the main branch may be lost. The latter is extended for the second time on the basis of the former result to better display the details of coronary arteries.

In order to quantitatively evaluate and compare the accuracy of the vessel segmentation results by each method, the correctness is expressed by means of *recall*, *precision* and their harmonic mean, the *F-Measure*, defined as[77]

$$\begin{aligned}
 recall &= \frac{TP}{TP + FN} \\
 precision &= \frac{TP}{TP + FP} \\
 F - Measure &= \frac{2 * recall * precision}{recall + precision}
 \end{aligned} \tag{37}$$

where TP (true positive) is the part of correctly classified foreground pixels, FP (false positive) is the part of background pixels that are wrongly classified as foreground, and FN (false negative) is the part of foreground pixels that are wrongly classified as backgrounds. Thus, *recall* reflects the ability to identify foreground pixels, *precision* reflects the correctness of classification, and *F-Measure* reflects the comprehensive performance of the segmentation method.

For clinical XCA image sequences and third-party database, we calculated *recall*, *precision* and *F-Measure* of different vessel segmentation methods and recorded them in Tab.3. And Fig.8 gives an intuitive distribution of the results for clinical images. Same as the experiment of foreground extraction, In this experiment, a frame was randomly selected for each image sequence, 7 clinical images and 10 database images were tested.

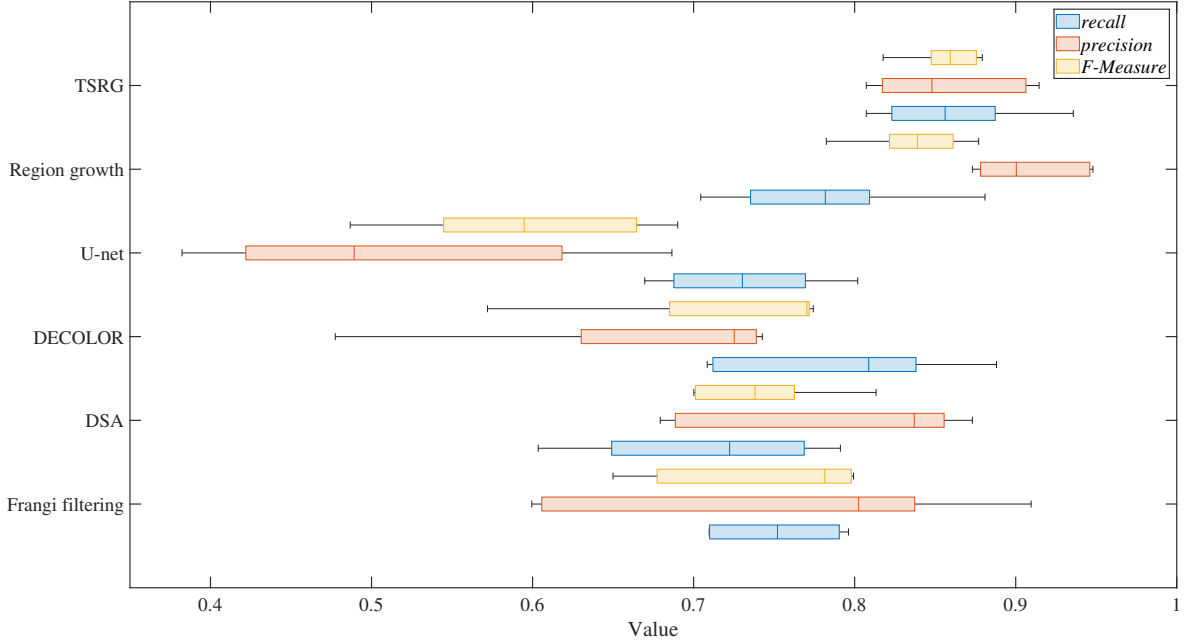


Figure 8: recall, precision and F-Measure values for clinical XCA images by different vessel segmentation methods.

Table 3: The mean recall, precision and F-Measure values (\pm standard deviation) of different vessel segmentation methods

Method	Clinical			Database		
	recall	precision	F-Measure	recall	precision	F-Measure
Frangi filtering	0.9513 \pm 0.0414	0.7465 \pm 0.1370	0.7429 \pm 0.0698	0.6471 \pm 0.0326	0.6859 \pm 0.0820	0.6622 \pm 0.0419
DSA	0.7085 \pm 0.0755	0.7862 \pm 0.0929	0.7397 \pm 0.0461	0.6188 \pm 0.0573	0.7253 \pm 0.0670	0.6617 \pm 0.0303
DECOLOR	0.7880 \pm 0.0766	0.6728 \pm 0.1119	0.7221 \pm 0.0866	0.7245 \pm 0.0498	0.5732 \pm 0.0831	0.6424 \pm 0.0511
U-net	0.7308 \pm 0.0523	0.5177 \pm 0.1230	0.5984 \pm 0.0797	0.6514 \pm 0.0309	0.3794 \pm 0.0962	0.4791 \pm 0.0524
Region growing	0.7796 \pm 0.0654	0.9093 \pm 0.0355	0.8378 \pm 0.0351	0.7340 \pm 0.0447	0.8589 \pm 0.0275	0.7826 \pm 0.0233
TSRG	0.8597 \pm 0.0492	0.8588 \pm 0.0484	0.8576 \pm 0.0242	0.8002 \pm 0.0314	0.8435 \pm 0.0382	0.8172 \pm 0.0198

3.5. Overall Discussion

In the previous experiments of TV-TRPCA and TSRG methods, we demonstrated the superiority of this study by the visibility of foreground extraction and the accuracy of vessel segmentation. On the one hand, compared with RPCA-based layer separation methods, due to the high-order information recovery ability of TRPCA and the constraint of TV on the foreground, the proposed method TV-TRPCA performs better in both the low-rank property of background and the spatial-temporal continuity of foreground with higher Global and Local CNR values. On the other hand, the proposed TSRG method segments the vessel layer in two stages. This improves the ability to present details while ensuring accuracy, and the continuity and integrity of vessels are preserved. Finally, binary coronary artery mask images with unique tubular structure are extracted completely.

4. Conclusion

A robust implementation of foreground extraction and vessel segmentation for X-ray coronary angiography image sequence is proposed in this paper. In clinical medicine, raw XCA images with irrelevant tissues, organ overlaps and high-frequency noise are difficult to use directly for pre-operative diagnosis. The existing vessel extraction methods such as Hessian based filtering, digital subtraction angiography (DSA) and robust principal component analysis (RPCA) have many shortcomings, like remaining irrelevant tissues, amplifying local noise and destroying high-dimensional information. To address these issues, in this study, the vessel extraction step is divided into two steps: foreground extraction and vessel segmentation.

In foreground extraction, a tensor nuclear norm (TNN) minimization based tensor robust principal component analysis (TRPCA) method is proposed and derived. In contrast to RPCA methods, TRPCA operates directly on the raw data form, which preserves more high-dimensional information. Total variation (TV) regularization is introduced to further enhance the spatial-temporal continuity of the foreground layer. In vessel segmentation, a two-stage region growing (TSRG) method is presented. In the first stage, a global threshold segmentation is used as preprocessing to obtain the main branch and remove the residual low-grayscale noise. In the second stage, the Radon-like filtering (RLF) is utilized to enhance the minor vessel segments, and the two parts are reconnected by region growing to get final coronary artery mask image. Experiments on clinical XCA image sequences and third-party database qualitatively and quantitatively demonstrate the high visibility of the vessel foregrounds extracted by TV-TRPCA and the high accuracy of the binary vessel masks segmented by TSRG.

The results of this study can serve as a theoretical basis for other quantitative analyses of coronary artery angiography images. For example, vessel centerline extraction and calibration. It is more accurate and efficient to extract the centerline from the binary vessel mask than directly from the raw XCA grayscale image. In addition, it provides a prerequisite for interventional path planning for guidewire operation. Another important application of this study is the 2D-3D registration of intra-operative X-ray angiography images with a 3D model constructed from pre-operative CT angiography. Our method improves the Signal-to-noise ratio (SNR) of XCA images and significantly enhances the visibility of vessel areas, thus improving the robustness, accuracy and real-time performance of 2D-3D registration.

Appendix A. Proof of Eq.30 in \mathcal{H} sub-problem

Eq.28 can be rewritten as

$$\mathbf{A}f(\mathcal{H}_{k+1}) = f(\mathcal{K}) \quad (\text{A.1})$$

where

$$\mathbf{A} = \left(\mu_k \mathbf{I} + \nu_k \left(\sigma_m^2 \mathbf{D}_m^T \mathbf{D}_m + \sigma_n^2 \mathbf{D}_n^T \mathbf{D}_n + \sigma_t^2 \mathbf{D}_t^T \mathbf{D}_t \right) \right) \quad (\text{A.2})$$

$\mathbf{D}_m, \mathbf{D}_n, \mathbf{D}_t \in \mathbb{R}^{MNT \times MNT}$ are block circulant matrices and $f(\mathcal{H}_{k+1}), f(\mathcal{K}) \in \mathbb{R}^{MNT}$ are tensor vectorization of \mathcal{H}_{k+1} and \mathcal{K} .

Consider the following equation

$$(\mathbf{I} + \mathbf{B}^T \mathbf{B})\mathbf{x} = \mathbf{y} \quad (\text{A.3})$$

where \mathbf{B} is a block circulant matrix, \mathbf{x} and \mathbf{y} are column vectors. It can be regarded as a simplified version of Eq.A.1.

According to matrix transformation theories[72, 71], \mathbf{B} can be diagonalized by the DFT matrix \mathbf{F} , i.e.,

$$\mathbf{B} = \mathbf{F}^H \mathbf{\Lambda} \mathbf{F} \quad (\text{A.4})$$

where \mathbf{F}^H is the Hermitian conjugate matrix of \mathbf{F} and $\mathbf{\Lambda} = \text{diagm}(\text{fft}(\mathbf{B}(:, 1)))$ forms a diagonal matrix storing the eigenvalues of \mathbf{B} . Notice that $\mathbf{F}^H \mathbf{F} = \mathbf{F} \mathbf{F}^H = \mathbf{I}$, Eq.A.3 can be rewritten as

$$\mathbf{F}^H (\mathbf{I} + \mathbf{\Lambda}^T \mathbf{\Lambda}) \mathbf{F} \mathbf{x} = \mathbf{y} \quad (\text{A.5})$$

Multiplying both sides of above equation by \mathbf{F} , it can be further rewritten as

$$\begin{aligned} (\mathbf{I} + \mathbf{\Lambda}^T \mathbf{\Lambda}) \mathbf{F} \mathbf{x} &= \mathbf{F} \mathbf{y} \\ \Rightarrow (\mathbf{I} + |\mathbf{\Lambda}|^2) \text{fft}(\mathbf{x}) &= \text{fft}(\mathbf{y}) \end{aligned} \quad (\text{A.6})$$

Since $\mathbf{I} + |\mathbf{\Lambda}|^2$ is a diagonal matrix, Eq.A.3 has the following solution

$$\mathbf{x} = \text{ifft} \left(\frac{\text{fft}(\mathbf{y})}{\text{diagv}(\mathbf{I} + |\mathbf{\Lambda}|^2)} \right) \quad (\text{A.7})$$

where $\text{diagv}(\cdot)$ forms a column vector from the elements of the diagonal of a matrix, $|\cdot|^2$ is the element-wise square, and the division is also performed element-wisely.

It is not hard to find that Eq.A.1 has a similar form with Eq.A.3, its solution Eq.30 can be derived by analogy.

Acknowledgment

This work was greatly supported by the National Natural Science Foundation of China (Grant No. 61973210) and the Medical-engineering Cross Projects of SJTU (Grant No. YG2019ZDA17, ZH2018QNB23). The authors would like to thank the doctors of Ruijin Hospital affiliated to Shanghai Jiao Tong University for their helps, and all the authors of open-source codes and database used in this study.

References

- [1] W. H. Organization, et al., World health statistics 2021, Tech. rep., World Health Organization (2021).
- [2] F. Valentin, Hurst's the Heart, (2 Volume Set), McGraw-Hill Medical, 2011.
- [3] W. Grossman, Grossman's cardiac catheterization, angiography, and intervention, Lippincott Williams & Wilkins, 2006.
- [4] H. Kirişli, M. Schaap, C. Metz, A. Dharampal, W. B. Meijboom, S.-L. Papadopoulou, A. Dedic, K. Nieman, M. A. de Graaf, M. Meijs, et al., Standardized evaluation framework for evaluating coronary artery stenosis detection, stenosis quantification and lumen segmentation algorithms in computed tomography angiography, Medical image analysis 17 (8) (2013) 859–876.

- [5] F. Bourier, A. Brost, L. Yatziv, J. Hornegger, N. Strobel, K. Kurzydum, A. Siemens, F. Bourier, Coronary sinus extraction for multimodality registration to guide transseptal puncture, in: 8th Interventional MRI Symposium, Leipzig, Citeseer, 2010, pp. 311–313.
- [6] C. B. Compas, T. Syeda-Mahmood, P. McNeillie, D. Beymer, Automatic detection of coronary stenosis in x-ray angiography through spatio-temporal tracking, in: 2014 IEEE 11th international symposium on biomedical imaging (ISBI), IEEE, 2014, pp. 1299–1302.
- [7] C. Sui, Z. Fu, Z. Fu, Y. Wang, Y. Zhuang, R. Xie, Y. Zhao, J. Zhang, J. Fei, A novel method for vessel segmentation and automatic diagnosis of vascular stenosis, in: 2019 IEEE International Conference on Robotics and Biomimetics (ROBIO), IEEE, 2019, pp. 918–923.
- [8] J. Guo, Y. Cheng, S. Guo, W. Du, A novel path planning algorithm for the vascular interventional surgical robotic doctor training system, in: 2017 IEEE International Conference on Mechatronics and Automation (ICMA), IEEE, 2017, pp. 45–50.
- [9] J. Yang, Y. Wang, Y. Liu, S. Tang, W. Chen, Novel approach for 3-d reconstruction of coronary arteries from two uncalibrated angiographic images, *Ieee transactions on image processing* 18 (7) (2009) 1563–1572.
- [10] Z. Fu, Z. Fu, Z. Gong, X. Feng, H. Gu, R. Xie, J. Zhang, J. Fei, Optimization for 3d reconstruction of coronary artery tree by two-stage levenberg-marquardt algorithm, in: 2021 27th International Conference on Mechatronics and Machine Vision in Practice (M2VIP), IEEE, 2021, pp. 84–89.
- [11] H. C. Lowe, S. N. Oesterle, L. M. Khachigian, Coronary in-stent restenosis: current status and future strategies, *Journal of the American College of Cardiology* 39 (2) (2002) 183–193.
- [12] D. L. Fischman, M. B. Leon, D. S. Baim, R. A. Schatz, M. P. Savage, I. Penn, K. Detre, L. Veltri, D. Ricci, M. Nobuyoshi, et al., A randomized comparison of coronary-stent placement and balloon angioplasty in the treatment of coronary artery disease, *New England Journal of Medicine* 331 (8) (1994) 496–501.
- [13] C. Lu, J. Feng, Y. Chen, W. Liu, Z. Lin, S. Yan, Tensor robust principal component analysis with a new tensor nuclear norm, *IEEE transactions on pattern analysis and machine intelligence* 42 (4) (2019) 925–938.
- [14] S. Moccia, E. De Momi, S. El Hadji, L. S. Mattos, Blood vessel segmentation algorithms—review of methods, datasets and evaluation metrics, *Computer methods and programs in biomedicine* 158 (2018) 71–91.
- [15] A. F. Frangi, W. J. Niessen, K. L. Vincken, M. A. Viergever, Multiscale vessel enhancement filtering, in: *International conference on medical image computing and computer-assisted intervention*, Springer, 1998, pp. 130–137.
- [16] Y. Sato, S. Nakajima, N. Shiraga, H. Atsumi, S. Yoshida, T. Koller, G. Gerig, R. Kikinis, Three-dimensional multi-scale line filter for segmentation and visualization of curvilinear structures in medical images, *Medical image analysis* 2 (2) (1998) 143–168.
- [17] M. Erdt, M. Raspe, M. Suehling, Automatic hepatic vessel segmentation using graphics hardware, in: *International workshop on medical imaging and virtual reality*, Springer, 2008, pp. 403–412.
- [18] R. Kumar, A. Vázquez-Reina, H. Pfister, Radon-like features and their application to connectomics, in: 2010 IEEE computer society conference on computer vision and pattern recognition-workshops, IEEE, 2010, pp. 186–193.
- [19] T. Syeda-Mahmood, F. Wang, R. Kumar, D. Beymer, Y. Zhang, R. Lundstrom, E. McNulty, Finding similar 2d x-ray coronary angiograms, in: *International Conference on Medical Image Computing and Computer-Assisted Intervention*, Springer, 2012, pp. 501–508.
- [20] N. Otsu, A threshold selection method from gray-level histograms, *IEEE transactions on systems, man, and cybernetics* 9 (1) (1979) 62–66.
- [21] A. K. Wong, P. K. Sahoo, A gray-level threshold selection method based on maximum entropy principle, *IEEE Transactions on Systems, Man, and Cybernetics* 19 (4) (1989) 866–871.
- [22] Y. Cheng, X. Hu, J. Wang, Y. Wang, S. Tamura, Accurate vessel segmentation with constrained b-snake, *IEEE Transactions on Image Processing* 24 (8) (2015) 2440–2455.
- [23] T. Lv, G. Yang, Y. Zhang, J. Yang, Y. Chen, H. Shu, L. Luo, Vessel segmentation using centerline constrained level set method, *Multimedia Tools and Applications* 78 (12) (2019) 17051–17075.
- [24] B. Van Ginneken, A. F. Frangi, J. J. Staal, B. M. ter Haar Romeny, M. A. Viergever, Active shape model segmentation with optimal features, *IEEE transactions on medical imaging* 21 (8) (2002) 924–933.
- [25] A. Kerkeni, A. Benabdallah, A. Manzanera, M. H. Bedoui, A coronary artery segmentation method based on multiscale analysis and region growing, *Computerized Medical Imaging and Graphics* 48 (2016) 49–61.

- [26] O. Friman, M. Hindennach, C. Kühnel, H.-O. Peitgen, Multiple hypothesis template tracking of small 3d vessel structures, *Medical image analysis* 14 (2) (2010) 160–171.
- [27] Y.-z. Zeng, Y.-q. Zhao, P. Tang, M. Liao, Y.-x. Liang, S.-h. Liao, B.-j. Zou, Liver vessel segmentation and identification based on oriented flux symmetry and graph cuts, *Computer methods and programs in biomedicine* 150 (2017) 31–39.
- [28] J. Long, E. Shelhamer, T. Darrell, Fully convolutional networks for semantic segmentation, in: *Proceedings of the IEEE conference on computer vision and pattern recognition*, 2015, pp. 3431–3440.
- [29] J. Fan, J. Yang, Y. Wang, S. Yang, D. Ai, Y. Huang, H. Song, A. Hao, Y. Wang, Multichannel fully convolutional network for coronary artery segmentation in x-ray angiograms, *Ieee Access* 6 (2018) 44635–44643.
- [30] O. Ronneberger, P. Fischer, T. Brox, U-net: Convolutional networks for biomedical image segmentation, in: *International Conference on Medical image computing and computer-assisted intervention*, Springer, 2015, pp. 234–241.
- [31] A. Vlontzos, K. Mikolajczyk, Deep segmentation and registration in x-ray angiography video, *arXiv preprint arXiv:1805.06406* (2018).
- [32] T. F. Meaney, M. Weinstein, E. Buonocore, W. Pavlicek, G. P. Borkowski, J. H. Gallagher, B. Sufka, W. J. MacIntyre, Digital subtraction angiography of the human cardiovascular system, in: *Application of Optical Instrumentation in Medicine VIII*, Vol. 233, SPIE, 1980, pp. 272–278.
- [33] Y. Bentoutou, N. Taleb, M. C. El Mezouar, M. Taleb, L. Jetto, An invariant approach for image registration in digital subtraction angiography, *Pattern Recognition* 35 (12) (2002) 2853–2865.
- [34] Y. Bentoutou, N. Taleb, A 3-d space–time motion detection for an invariant image registration approach in digital subtraction angiography, *Computer Vision and Image Understanding* 97 (1) (2005) 30–50.
- [35] M. Yamamoto, Y. Okura, M. Ishihara, M. Kagemoto, K. Harada, T. Ishida, Development of digital subtraction angiography for coronary artery, *Journal of digital imaging* 22 (3) (2009) 319–325.
- [36] S. Song, J. Yang, D. Ai, C. Du, Y. Huang, H. Song, L. Zhang, Y. Han, Y. Wang, A. F. Frangi, Patch-based adaptive background subtraction for vascular enhancement in x-ray cineangiograms, *IEEE journal of biomedical and health informatics* 23 (6) (2019) 2563–2575.
- [37] E. Nasr-Esfahani, S. Samavi, N. Karimi, S. R. Soroushmehr, K. Ward, M. H. Jafari, B. Felfeliyan, B. Nallamothu, K. Najarian, Vessel extraction in x-ray angiograms using deep learning, in: *2016 38th Annual international conference of the IEEE engineering in medicine and biology society (EMBC)*, IEEE, 2016, pp. 643–646.
- [38] H. Hao, H. Ma, T. van Walsum, Vessel layer separation in x-ray angiograms with fully convolutional network, in: *Medical imaging 2018: Image-guided procedures, robotic interventions, and modeling*, Vol. 10576, International Society for Optics and Photonics, 2018, p. 105761V.
- [39] H. Hao, Vessel layer separation of x-ray angiographic images using deep learning methods, [EB/OL], <http://resolver.tudelft.nl/uuid:ae819077-c7cd-4737-ad6e-7289cb39e3bd> (2018).
- [40] S. Tang, Y. Wang, Y.-W. Chen, Application of ica to x-ray coronary digital subtraction angiography, *Neurocomputing* 79 (2012) 168–172.
- [41] S. Xia, H. Zhu, X. Liu, M. Gong, X. Huang, L. Xu, H. Zhang, J. Guo, Vessel segmentation of x-ray coronary angiographic image sequence, *IEEE Transactions on Biomedical Engineering* 67 (5) (2019) 1338–1348.
- [42] E. J. Candès, X. Li, Y. Ma, J. Wright, Robust principal component analysis?, *Journal of the ACM (JACM)* 58 (3) (2011) 1–37.
- [43] J. Wright, A. Ganesh, S. Rao, Y. Peng, Y. Ma, Robust principal component analysis: Exact recovery of corrupted low-rank matrices via convex optimization, *Advances in neural information processing systems* 22 (2009).
- [44] H. Ma, G. Dibildox, J. Banerjee, W. Niessen, C. Schultz, E. Regar, T. v. Walsum, Layer separation for vessel enhancement in interventional x-ray angiograms using morphological filtering and robust pca, in: *Workshop on Augmented Environments for Computer-Assisted Interventions*, Springer, 2015, pp. 104–113.
- [45] H. Ma, A. Hoogendoorn, E. Regar, W. J. Niessen, T. van Walsum, Automatic online layer separation for vessel enhancement in x-ray angiograms for percutaneous coronary interventions, *Medical image analysis* 39 (2017) 145–161.
- [46] J. Zhang, G. Wang, H. Xie, S. Zhang, Z. Shi, L. Gu, Vesselness-constrained robust pca for vessel enhancement in x-ray coronary angiograms, *Physics in Medicine & Biology* 63 (15) (2018) 155019.
- [47] B. Qin, M. Jin, D. Hao, Y. Lv, Q. Liu, Y. Zhu, S. Ding, J. Zhao, B. Fei, Accurate vessel extraction via tensor completion of background layer

- in x-ray coronary angiograms, *Pattern recognition* 87 (2019) 38–54.
- [48] S. Song, C. Du, D. Ai, Y. Huang, H. Song, Y. Wang, J. Yang, Spatio-temporal constrained online layer separation for vascular enhancement in x-ray angiographic image sequence, *IEEE Transactions on Circuits and Systems for Video Technology* 30 (10) (2019) 3558–3570.
- [49] T. G. Kolda, B. W. Bader, Tensor decompositions and applications, *SIAM review* 51 (3) (2009) 455–500.
- [50] M. E. Kilmer, K. Braman, N. Hao, R. C. Hoover, Third-order tensors as operators on matrices: A theoretical and computational framework with applications in imaging, *SIAM Journal on Matrix Analysis and Applications* 34 (1) (2013) 148–172.
- [51] Z. Zhang, G. Ely, S. Aeron, N. Hao, M. Kilmer, Novel methods for multilinear data completion and de-noising based on tensor-svd, in: *Proceedings of the IEEE conference on computer vision and pattern recognition*, 2014, pp. 3842–3849.
- [52] D. Goldfarb, Z. Qin, Robust low-rank tensor recovery: Models and algorithms, *SIAM Journal on Matrix Analysis and Applications* 35 (1) (2014) 225–253.
- [53] Q. Xie, Q. Zhao, D. Meng, Z. Xu, Kronecker-basis-representation based tensor sparsity and its applications to tensor recovery, *IEEE transactions on pattern analysis and machine intelligence* 40 (8) (2017) 1888–1902.
- [54] Y. Liu, L. Chen, C. Zhu, Improved robust tensor principal component analysis via low-rank core matrix, *IEEE Journal of Selected Topics in Signal Processing* 12 (6) (2018) 1378–1389.
- [55] D. Driggs, S. Becker, J. Boyd-Graber, Tensor robust principal component analysis: Better recovery with atomic norm regularization, *arXiv preprint arXiv:1901.10991* (2019).
- [56] C. Lu, J. Feng, Y. Chen, W. Liu, Z. Lin, S. Yan, Tensor robust principal component analysis: Exact recovery of corrupted low-rank tensors via convex optimization, in: *Proceedings of the IEEE conference on computer vision and pattern recognition*, 2016, pp. 5249–5257.
- [57] Q. Gao, P. Zhang, W. Xia, D. Xie, X. Gao, D. Tao, Enhanced tensor rpca and its application, *IEEE Transactions on Pattern Analysis and Machine Intelligence* 43 (6) (2020) 2133–2140.
- [58] Y. Xie, S. Gu, Y. Liu, W. Zuo, W. Zhang, L. Zhang, Weighted Schatten p -norm minimization for image denoising and background subtraction, *IEEE transactions on image processing* 25 (10) (2016) 4842–4857.
- [59] S. H. Chan, R. Khoshabeh, K. B. Gibson, P. E. Gill, T. Q. Nguyen, An augmented Lagrangian method for total variation video restoration, *IEEE Transactions on Image Processing* 20 (11) (2011) 3097–3111.
- [60] W. Cao, Y. Wang, J. Sun, D. Meng, C. Yang, A. Cichocki, Z. Xu, Total variation regularized tensor rpca for background subtraction from compressive measurements, *IEEE Transactions on Image Processing* 25 (9) (2016) 4075–4090.
- [61] Y. Wang, J. Peng, Q. Zhao, Y. Leung, X.-L. Zhao, D. Meng, Hyperspectral image restoration via total variation regularized low-rank tensor decomposition, *IEEE Journal of Selected Topics in Applied Earth Observations and Remote Sensing* 11 (4) (2017) 1227–1243.
- [62] B. E. Moore, C. Gao, R. R. Nadakuditi, Panoramic robust PCA for foreground–background separation on noisy, free-motion camera video, *IEEE Transactions on Computational Imaging* 5 (2) (2019) 195–211.
- [63] Y.-T. Wang, X.-L. Zhao, T.-X. Jiang, L.-J. Deng, T.-H. Ma, Y.-T. Zhang, T.-Z. Huang, A total variation and group sparsity based tensor optimization model for video rain streak removal, *Signal Processing: Image Communication* 73 (2019) 96–108.
- [64] M. Jin, R. Li, J. Jiang, B. Qin, Extracting contrast-filled vessels in x-ray angiography by graduated rpca with motion coherency constraint, *Pattern Recognition* 63 (2017) 653–666.
- [65] M. E. Kilmer, C. D. Martin, Factorization strategies for third-order tensors, *Linear Algebra and its Applications* 435 (3) (2011) 641–658.
- [66] L. I. Rudin, S. Osher, E. Fatemi, Nonlinear total variation based noise removal algorithms, *Physica D: nonlinear phenomena* 60 (1-4) (1992) 259–268.
- [67] Q. Zhao, D. Meng, Z. Xu, W. Zuo, L. Zhang, Robust principal component analysis with complex noise, in: *International conference on machine learning*, PMLR, 2014, pp. 55–63.
- [68] Z. Lin, A. Ganesh, J. Wright, L. Wu, M. Chen, Y. Ma, Fast convex optimization algorithms for exact recovery of a corrupted low-rank matrix, *Coordinated Science Laboratory Report no. UILU-ENG-09-2214, DC-246* (2009).
- [69] Z. Lin, M. Chen, Y. Ma, The augmented Lagrange multiplier method for exact recovery of corrupted low-rank matrices, *arXiv preprint arXiv:1009.5055* (2010).

- [70] X. Yuan, J. Yang, Sparse and low-rank matrix decomposition via alternating direction methods, preprint 12 (2) (2009).
- [71] R. M. Gray, Toeplitz and circulant matrices: A review, *Foundations and Trends in Communications and Information Theory* 2 (3) (2006) 155–239.
- [72] G. H. Golub, C. F. Van Loan, *Matrix computations*, JHU press, 2013.
- [73] R. Adams, L. Bischof, Seeded region growing, *IEEE Transactions on pattern analysis and machine intelligence* 16 (6) (1994) 641–647.
- [74] A. Tremeau, N. Borel, A region growing and merging algorithm to color segmentation, *Pattern recognition* 30 (7) (1997) 1191–1203.
- [75] H. Cai, J.-F. Cai, K. Wei, Accelerated alternating projections for robust principal component analysis, *The Journal of Machine Learning Research* 20 (1) (2019) 685–717.
- [76] X. Zhou, C. Yang, W. Yu, Moving object detection by detecting contiguous outliers in the low-rank representation, *IEEE transactions on pattern analysis and machine intelligence* 35 (3) (2012) 597–610.
- [77] S. Brutzer, B. Höferlin, G. Heidemann, Evaluation of background subtraction techniques for video surveillance, in: *CVPR 2011, IEEE, 2011*, pp. 1937–1944.